

Benchmarking the Fully Relativistic Collision Operator in CQL3D

Yuri Petrov and R.W.Harvey, *CompX, Del Mar, California, Report CompX-2009-1, Oct.16,2009*

The fully relativistic collision operator in CQL3D code is updated and tested in different applications. The operator is benchmarked against the quasi-relativistic operator in CQL3D, and against the fully relativistic operator in the ADJ code.

I. BACKGROUND

In general form, the collision operator is written as [1, 2]

$$C_{ab} = \frac{\partial}{\partial \mathbf{v}} \cdot \left[\mathbf{D}_{ab} \cdot \frac{\partial f_a(\mathbf{v})}{\partial \mathbf{v}} - \mathbf{F}_{ab} f_a(\mathbf{v}) \right], \quad (1)$$

where \mathbf{v} is the momentum per rest mass, and \mathbf{D}_{ab} and \mathbf{F}_{ab} are the diffusion and friction coefficients,

$$\mathbf{D}_{ab}(\mathbf{v}) = \frac{1}{2} \Gamma_a \sum_b \left(\frac{Z_b}{Z_a} \right)^2 \ln \Lambda_{ab} \int \mathbf{U}(\mathbf{v}, \mathbf{v}') f_b(\mathbf{v}') d^3 v' \quad (2)$$

$$\mathbf{F}_{ab}(\mathbf{v}) = -\frac{1}{2} \Gamma_a \sum_b \left(\frac{Z_b}{Z_a} \right)^2 \frac{m_a}{m_b} \ln \Lambda_{ab} \int \left(\frac{\partial}{\partial \mathbf{v}'} \cdot \mathbf{U}(\mathbf{v}, \mathbf{v}') \right) f_b(\mathbf{v}') d^3 v'. \quad (3)$$

Here, $\Gamma_a = 4\pi Z_a^4 e^4 / m_a^2$, if cgs units are used.

In the non-relativistic limit, the momentum per rest mass \mathbf{v} reduces to velocity \mathbf{u} . The kernel \mathbf{U} has the shape [1]

$$\mathbf{U}_{nr} = \frac{|\mathbf{s}|^2 \mathbf{I} - \mathbf{s}\mathbf{s}}{|\mathbf{s}|^3}, \quad (4)$$

where $\mathbf{s} = \mathbf{u} - \mathbf{u}'$. It can be seen that

$$\mathbf{U}_{nr} = \frac{\partial}{\partial \mathbf{u}} \frac{\partial |\mathbf{s}|}{\partial \mathbf{u}}, \quad (5)$$

and

$$\frac{\partial}{\partial \mathbf{u}'} \cdot \mathbf{U}_{nr} = -2 \frac{\partial}{\partial \mathbf{u}} \frac{1}{|\mathbf{s}|}. \quad (6)$$

The latter equation allows changing the differentiation over \mathbf{u}' in Eq. (3) to differentiation over \mathbf{u} and moving it outside of the integral. By introducing ‘potentials’ [3, 4]

$$h(\mathbf{u}) = -\frac{1}{8\pi} \int |\mathbf{s}| f_b d^3 u', \quad (7)$$

$$g(\mathbf{u}) = -\frac{1}{4\pi} \int |\mathbf{s}|^{-1} f_b d^3 u', \quad (8)$$

the diffusion coefficient can be written through $\partial^2 h / \partial \mathbf{u} \partial \mathbf{u}$, and the friction coefficient – through $\partial g / \partial \mathbf{u}$. The non-relativistic collision operator is one of the options in CQL3D.

For relativistic particles, an approximate description of collision operator ('quasi-relativistic operator') is obtained [5] when the kernel is taken in the shape given by Eq. (4), but integration in Eqs. (2-3) is performed over relativistic momentum. By introducing 'potentials'

$$h_a(\mathbf{v}) = \sum_b \left(\frac{Z_b}{Z_a} \right)^2 \frac{m_a}{m_b} \ln \Lambda_{ab} \int \frac{|\mathbf{u} - \mathbf{u}'|}{\gamma'} f_b(\mathbf{v}') d^3 v', \quad (9)$$

$$g_a(\mathbf{v}) = \sum_b \left(\frac{Z_b}{Z_a} \right)^2 \ln \Lambda_{ab} \int |\mathbf{u} - \mathbf{u}'| f_b(\mathbf{v}') d^3 v', \quad (10)$$

the collision operator is expressed as

$$C_{ab} = \frac{1}{2} \Gamma_a \frac{\partial}{\partial \mathbf{v}} \cdot \left[\frac{\partial}{\partial \mathbf{u}} \left(\frac{\partial g_a}{\partial \mathbf{u}} \right) \cdot \frac{\partial f_a(\mathbf{v})}{\partial \mathbf{v}} - f_a(\mathbf{v}) \frac{\partial}{\partial \mathbf{u}} \left(\gamma \frac{\partial}{\partial \mathbf{v}} \cdot \frac{\partial h_a}{\partial \mathbf{u}} \right) \right]. \quad (11)$$

The values of \mathbf{u} (velocity) and \mathbf{v} (momentum per rest mass) in Eqs. (9-11) are related through $\mathbf{u} = \mathbf{v} / \gamma$, (12)

or

$$\mathbf{v} = \frac{\mathbf{u}}{\left(1 - |\mathbf{u}|^2 / c^2 \right)^{1/2}}, \quad (13)$$

where $\gamma = \sqrt{1 + |\mathbf{v}|^2 / c^2}$. Further, the distribution function is expanded in Legendre polynomials,

$$f_b(v, \theta) = \sum_{l=0}^{\infty} V_l^b(v) P_l(\cos \theta), \quad (14)$$

leading to expressions for h_a and g_a in terms of integrals like [5]

$$M_l = \int_v \frac{V_l^b(v')}{\gamma'} u'^{(1-l)} \gamma'^2 dv'. \quad (15)$$

Effectively, the primed and non-primed variables in Eqs. (9-10) become decoupled. The quasi-relativistic collision operator is another option in CQL3D.

The strict formulation for the relativistic collision operator is based on the fully-relativistic kernel [2],

$$\mathbf{U}(\mathbf{v}, \mathbf{v}') = \frac{r^2}{c \gamma \gamma' (r^2 - 1)^{3/2}} \left[(r^2 - 1) \mathbf{I} - \boldsymbol{\alpha} \boldsymbol{\alpha} - \boldsymbol{\alpha}' \boldsymbol{\alpha}' + r(\boldsymbol{\alpha} \boldsymbol{\alpha}' + \boldsymbol{\alpha}' \boldsymbol{\alpha}) \right], \quad (16)$$

where $\boldsymbol{\alpha} = \mathbf{v}/c$ and $r = \gamma \gamma' - \boldsymbol{\alpha} \cdot \boldsymbol{\alpha}'$. (note, $\boldsymbol{\alpha} \boldsymbol{\alpha}$ is a matrix, and $\boldsymbol{\alpha} \cdot \boldsymbol{\alpha}' = \alpha \alpha' \cos(\theta - \theta')$ is a scalar, where θ is the pitch-angle in \mathbf{v} -space). In the non-relativistic limit, $r \rightarrow 1$, $\sqrt{r^2 - 1} \rightarrow |\mathbf{u} - \mathbf{u}'|/c$, and \mathbf{U} reverts to the form of Eq. (4).

The diffusion and friction coefficients are expressed as [6]

$$\mathbf{D}_{ab} = \frac{2}{\gamma} \mathbf{L} \Psi_1 + \frac{1}{\gamma c^2} [\mathbf{I} + \boldsymbol{\alpha} \boldsymbol{\alpha}] \Psi_2, \quad (17)$$

$$\mathbf{F}_{ab} = \frac{2}{\gamma} \mathbf{K} \Psi_3, \quad (18)$$

where \mathbf{L} and \mathbf{K} operators are [7, 8]

$$\mathbf{L} \Psi(\mathbf{v}) = (\mathbf{I} + \boldsymbol{\alpha} \boldsymbol{\alpha}) \left(\frac{\partial}{\partial \mathbf{v}} \left(\frac{\partial \Psi}{\partial \mathbf{v}} \right) \right) (\mathbf{I} + \boldsymbol{\alpha} \boldsymbol{\alpha}) + \frac{1}{c^2} (\mathbf{I} + \boldsymbol{\alpha} \boldsymbol{\alpha}) \left(\mathbf{v} \cdot \frac{\partial \Psi}{\partial \mathbf{v}} \right), \quad (19)$$

$$\mathbf{K}\Psi(\mathbf{v}) = (\mathbf{I} + \mathbf{a}\mathbf{a}) \frac{\partial \Psi}{\partial \mathbf{v}}. \quad (20)$$

The ‘potentials’ Ψ_1, Ψ_2, Ψ_3 are expressed through the distribution function f_b of background species as

$$\Psi_1(\mathbf{v}) = c\Gamma_a \sum_b \left(\frac{Z_b}{Z_a} \right)^2 \ln \Lambda_{ab} \int \left(\xi_1(r) - \frac{1}{2} \xi_2(r) \right) f_b(\mathbf{v}') d\mathbf{v}' / \gamma' \quad (21)$$

$$\Psi_2(\mathbf{v}) = c\Gamma_a \sum_b \left(\frac{Z_b}{Z_a} \right)^2 \ln \Lambda_{ab} \int \xi_2(r) f_b(\mathbf{v}') d\mathbf{v}' / \gamma' \quad (22)$$

$$\Psi_3(\mathbf{v}) = \frac{1}{c} \Gamma_a \sum_b \left(\frac{Z_b}{Z_a} \right)^2 \frac{m_a}{m_b} \ln \Lambda_{ab} \int \xi_3(r) f_b(\mathbf{v}') d\mathbf{v}' / \gamma' \quad (23)$$

where

$$\xi_1(r) = \sqrt{r^2 - 1} \quad (24)$$

$$\xi_2(r) = r \cosh^{-1}(r) \quad (25)$$

$$\xi_3(r) = \frac{r}{\sqrt{r^2 - 1}} - \cosh^{-1}(r). \quad (26)$$

Further, the distribution function of the background species and kernels of Ψ_1, Ψ_2, Ψ_3 are expanded in terms of Legendre polynomials,

$$f_b(v, \theta) = \sum_{l=0}^{\infty} V_l^b(v) P_l(\cos \theta) \quad (27)$$

$$\xi_n(r) = \sum_{l=0}^{\infty} \kappa_l^n(\alpha, \alpha') P_l(\cos(\theta - \theta')). \quad (28)$$

Recalling that $r = \gamma\gamma' - \mathbf{a} \cdot \mathbf{a}'$, the value of $\cos(\theta - \theta')$ can be expressed as

$$\cos(\theta - \theta') = \frac{\gamma\gamma' - r}{\alpha\alpha'}. \quad (29)$$

Then,

$$\begin{aligned} \kappa_l^n(\alpha, \alpha') &= \frac{2l+1}{2} \int_{-1}^1 \xi_n(r) P_l(\cos(\theta - \theta')) d(\cos(\theta - \theta')) = \\ &= -\frac{2l+1}{2} \int_{\gamma\gamma'+\alpha\alpha'}^{\gamma\gamma'-\alpha\alpha'} \xi_n(r) P_l\left(\frac{\gamma\gamma' - r}{\alpha\alpha'}\right) \frac{dr}{\alpha\alpha'}. \end{aligned} \quad (30)$$

Substituting the definition of P_l ,

$$P_l(x) = \frac{1}{2^l} \sum_{k=0}^{\lfloor l/2 \rfloor} (-1)^k \binom{l}{k} \binom{2l-2k}{l} x^{l-2k}, \quad (31)$$

where $\binom{l}{k} \equiv \frac{l!}{k!(l-k)!}$, results in

$$\kappa_l^n(\alpha, \alpha') = \frac{2l+1}{2^{l+1}} \sum_{k=0}^{\lfloor l/2 \rfloor} (-1)^k \binom{l}{k} \binom{2l-2k}{l} \int_{\gamma\gamma'-\alpha\alpha'}^{\gamma\gamma'+\alpha\alpha'} \xi_n(r) \left(\frac{\gamma\gamma' - r}{\alpha\alpha'} \right)^{l-2k} \frac{dr}{\alpha\alpha'}. \quad (32)$$

Performing the binomial expansion of $(\gamma\gamma' - r)^{-2k}$, one obtains

$$\kappa_l^n(\alpha, \alpha') = \frac{2l+1}{2} \sum_{k=0}^{\lfloor l/2 \rfloor} \sum_{j=0}^{l-2k} \eta_{lkj} \frac{(\gamma\gamma')^{l-2k-j}}{(\alpha\alpha')^{l-2k+1}} \int_{\gamma\gamma'-\alpha\alpha'}^{\gamma\gamma'+\alpha\alpha'} \xi_n(r) r^j dr, \quad (33)$$

where

$$\eta_{lkj} = \frac{(-1)^{k+j}}{2^l} \binom{l}{k} \binom{2l-2k}{l} \binom{l-2k}{j}. \quad (34)$$

The steps starting from Eq. (29) allow decoupling the primed and unprimed variables. However, it should be noted that this procedure also introduces a problem at the $\alpha \rightarrow 0$ or $\alpha' \rightarrow 0$ limit. The double sum in Eq. (33) contains divergent terms, while the original integral in Eq. (30) is not divergent at $r \rightarrow 1$ (although $\xi_3(r)$ is divergent at $r \rightarrow 1$, the integral is not). This observation implies the presence of large canceling terms in the double sum of Eq. (33). Such terms become a source of numerical noise and instabilities in the $|\mathbf{v}| \sim 0$ region of the momentum grid.

Continuing this procedure, the ‘potentials’ in Eqs. (21-23) are expressed as [6]

$$\begin{aligned} \Psi_1(\mathbf{v}) = & 2\pi c \Gamma_a \sum_b \left(\frac{Z_b}{Z_a} \right)^2 \ln \Lambda_{ab} \sum_{l=0}^{\infty} \sum_{k=0}^{\lfloor l/2 \rfloor} \sum_{j=0}^{l-2k} P_l(\cos \theta) \eta_{lkj} \times \\ & \times \left\{ \frac{1}{(j+1)} \psi_1^{j+1}(l-2k-j, l-2k+1) - \frac{1}{2(j+2)} \psi_2^{j+2}(l-2k-j, l-2k+1) \right. \\ & \left. - \frac{j+3}{2(j+1)(j+2)} \psi_3^{j+2}(l-2k-j, l-2k+1) \right\} \end{aligned} \quad (35)$$

$$\begin{aligned} \Psi_2(\mathbf{v}) = & 2\pi c \Gamma_a \sum_b \left(\frac{Z_b}{Z_a} \right)^2 \ln \Lambda_{ab} \sum_{l=0}^{\infty} \sum_{k=0}^{\lfloor l/2 \rfloor} \sum_{j=0}^{l-2k} P_l(\cos \theta) \eta_{lkj} \times \\ & \times \left\{ \frac{1}{(j+2)} \psi_2^{j+2}(l-2k-j, l-2k+1) - \frac{1}{(j+2)} \psi_3^{j+2}(l-2k-j, l-2k+1) \right\} \end{aligned} \quad (36)$$

$$\begin{aligned} \Psi_3(\mathbf{v}) = & \frac{2\pi}{c} \Gamma_a \sum_b \left(\frac{Z_b}{Z_a} \right)^2 \frac{m_a}{m_b} \ln \Lambda_{ab} \sum_{l=0}^{\infty} \sum_{k=0}^{\lfloor l/2 \rfloor} \sum_{j=0}^{l-2k} P_l(\cos \theta) \eta_{lkj} \times \\ & \times \left\{ -\frac{1}{(j+1)} \psi_2^{j+1}(l-2k-j, l-2k+1) + \frac{(j+2)}{(j+1)} \psi_3^{j+1}(l-2k-j, l-2k+1) \right\} \end{aligned} \quad (37)$$

Here, the functionals $\psi_{1,2}^j$ are

$$\begin{aligned} \psi_1^j(m, n) = & \\ = & 2 \sum_{i=0}^j \binom{j}{i} \frac{\gamma^{m+j-i}}{\alpha^{n-i}} \times \begin{cases} \gamma \chi_1^l(m+j-i, n-i-1) + \alpha \chi_2^l(m+j-i+1, n-i), & i \text{ even} \\ \gamma \chi_2^l(m+j-i, n-i-1) + \alpha \chi_1^l(m+j-i+1, n-i), & i \text{ odd} \end{cases} \end{aligned} \quad (38)$$

$$\begin{aligned} \psi_2^j(m, n) = & \\ = & 2 \sum_{i=0}^j \binom{j}{i} \frac{\gamma^{m+j-i}}{\alpha^{n-i}} \times \begin{cases} \sinh^{-1}(\alpha) \chi_2^l(m+j-i, n-i) + \chi_3^l(m+j-i, n-i), & i \text{ even} \\ \sinh^{-1}(\alpha) \chi_1^l(m+j-i, n-i) + \chi_4^l(m+j-i, n-i), & i \text{ odd} \end{cases} \end{aligned} \quad (39)$$

The third functional, ψ_3^j is a combination of the first two [6],

$$\psi_3^{2j}(m, n) = \frac{(2j)!}{2^{2j}(j!)^2} \left\{ \sum_{i=1}^j \frac{2^{2i-1} i!(i-1)!}{(2i)!} \psi_1^{2i-1}(m, n) + \psi_2^0(m, n) \right\}, \quad \text{for } (2j) \text{ - indices} \quad (40a)$$

$$\psi_3^{2j+1}(m, n) = \frac{2^{2j}(j!)^2}{(2j+1)!} \left\{ \sum_{i=0}^j \frac{(2i)!}{2^{2i}(i!)^2} \psi_1^{2i}(m, n) \right\}, \quad \text{for odd indices } (2j+1). \quad (40b)$$

The functions χ_n^l represent the integrals

$$\chi_1^l(m, n) = \int_0^v \gamma^{m-1} \alpha^{-n} V_l^b(v) v^2 dv \quad (41)$$

$$\chi_2^l(m, n) = \int_v^\infty \gamma^{m-1} \alpha^{-n} V_l^b(v) v^2 dv \quad (42)$$

$$\chi_3^l(m, n) = \int_0^v \gamma^{m-1} \alpha^{-n} \sinh^{-1}(\alpha) V_l^b(v) v^2 dv \quad (43)$$

$$\chi_4^l(m, n) = \int_v^\infty \gamma^{m-1} \alpha^{-n} \sinh^{-1}(\alpha) V_l^b(v) v^2 dv \quad (44)$$

The ‘potentials’ defined above are used to determine the local collision coefficients for the bounce-averaged Fokker-Planck equation,

$$A_c = -\mathcal{W}^2 \frac{\partial \Psi_3}{\partial v} \quad (45)$$

$$B_c = \gamma^2 v^2 \frac{\partial}{\partial v} \left(\gamma \frac{\partial \Psi_1}{\partial v} \right) + \frac{\mathcal{W}^2}{2c^2} \Psi_2 \quad (46)$$

$$C_c = \mathcal{W} \frac{\partial}{\partial v} \left(\frac{1}{v} \frac{\partial \Psi_1}{\partial \theta} \right) \quad (47)$$

$$D_c = -\frac{1}{\gamma} \sin \theta \frac{\partial \Psi_3}{\partial \theta} \quad (48)$$

$$E_c = \mathcal{W} \sin \theta \frac{\partial}{\partial v} \left(\frac{1}{v} \frac{\partial \Psi_1}{\partial \theta} \right) \quad (49)$$

$$F_c = \sin \theta \left(\frac{\gamma}{v} \frac{\partial \Psi_1}{\partial v} + \frac{1}{\mathcal{W}^2} \frac{\partial^2 \Psi_1}{\partial \theta^2} + \frac{1}{2\mathcal{W}^2} \Psi_2 \right). \quad (50)$$

The fully relativistic collision operator is the third option in CQL3D.

It should be mentioned that an alternative representation for the fully relativistic collision operator was obtained by Braams and Karney [7, 8]. They start with the same relativistic kernel as given by Eq. (16) and introduce five ‘potentials’, four of which are used to express the diffusion and friction coefficients; these four potentials could be combined into three potentials given above by Eqs. (35-37). The potentials are further expanded in terms of Legendre harmonics,

$$\Psi_{[k]^*}(\boldsymbol{\alpha}) = \sum_{l=0}^{\infty} \psi_{l[k]^*}(\alpha) P_l(\cos \theta). \quad (51)$$

It is shown that

$$\psi_{l[k]*}(\alpha) = c^3 \int_0^\alpha N_{l[k]*}(\alpha, \alpha') \frac{\alpha'^2}{\gamma'} V_l^b(\alpha') d\alpha', \quad (52)$$

where V_l^b is the coefficient in the expansion of the distribution function in Legendre harmonics, and functions $N_{l[k]*}$ are given by

$$N_{l[1]1}(\alpha, \alpha') = c^{-1} y_{l[1]1}(\alpha) j_{l[1]1}(\alpha') \quad (53)$$

$$N_{l[2]02}(\alpha, \alpha') = c y_{l[1]0}(\alpha) j_{l[2]02}(\alpha') + c y_{l[2]02}(\alpha) j_{l[1]2}(\alpha') \quad (54)$$

$$N_{l[2]11}(\alpha, \alpha') = c y_{l[1]1}(\alpha) j_{l[2]11}(\alpha') + c y_{l[2]11}(\alpha) j_{l[1]1}(\alpha') \quad (55)$$

$$N_{l[3]022}(\alpha, \alpha') = c^3 y_{l[1]0}(\alpha) j_{l[3]022}(\alpha') + c^3 y_{l[2]02}(\alpha) j_{l[2]22}(\alpha') + c^3 y_{l[3]022}(\alpha) j_{l[1]2}(\alpha'). \quad (56)$$

The functions $y_{l[k]*}$ and $j_{l[k]*}$ are defined through the associated Legendre functions of the first kind $P_\nu^\mu(\gamma)$ as

$$j_{l[1]a}(\alpha) = \sqrt{\frac{\pi}{2\alpha}} P_{a-1/2}^{-l-1/2}(\gamma), \quad (57)$$

$$y_{l[1]a}(\alpha) = (-1)^{-l-1} \sqrt{\frac{\pi}{2\alpha}} P_{a-1/2}^{l+1/2}(\gamma), \quad (58)$$

with higher- k functions defined recursively by

$$j_{l[k+2]*aa'} = \begin{cases} \frac{j_{l[k+1]*a} - j_{l[k+1]*a'}}{a^2 - a'^2}, & \text{for } a \neq a' \\ \frac{\partial j_{l[k+1]*a}}{\partial(a^2)}, & \text{for } a = a' \end{cases} \quad (59)$$

and similarly for $y_{l[k]*}$. This approach is implemented in the ADJ code which calculates the conductivity of relativistic plasma [8]. The ADJ code is used below for benchmarking the CQL3D code with conductivity tests.

II. GOALS

The main purpose of the current work is to debug and benchmark the fully relativistic operator in CQL3D. Presently, the code can be launched in three main modes: *relativ* = 'disabled', 'enabled', and 'fully', where *relativ* is the input parameter in *cqlinput* namelist. Those cases correspond to non-relativistic, quasi-relativistic, and fully-relativistic collision operators. The first two have been intensely used and benchmarked. The latter one is known to make the code unstable. For benchmarking, three types of tests are performed: Calculations of plasma conductivity, lower hybrid heating/current drive (LH), and electron cyclotron heating (ECH).

III. DEBUGGING, MODIFICATIONS, NUMERICAL PROBLEMS

After examining the code, several errors have been found. In subroutine *cfpcoefr*, which defines the fully relativistic operator, a bounds error is corrected. This error is related to definition of η_{lkj} coefficients. Another error is found in the index range for arrays *tamt1* and *tamt2*, which define

the integrals in Eqs. (41-44). In subroutine *micxinil*, the definition is added for $\gamma^{-1} \equiv \text{gamman}(j,-1)$, which is used in *cfpcoefr* for $j = 1$ velocity point. Before this, *gamman*($j,-1$) was defined for $j > 1$ only.

Further tests have shown that the *relativ=’fully’* mode results in a code crash if the temperature of plasma is below 5 keV, and the number of requested Legendre harmonics (*mx*) is higher than three. Numerical instability is seen to originate at small $|\mathbf{v}|$ in the distribution function. It is determined that the instability is caused by divergent terms in Eqs. (33, 38-40) at $|\mathbf{v}| \rightarrow 0$ ($\alpha \rightarrow 0$), as discussed in Section I. Although the functions given by Eqs. (38-44) are defined in the code starting from the *second* node of the \mathbf{v} -grid (thus avoiding $|\mathbf{v}| = 0$ point), the large canceling terms introduce increasing numerical error at grid points close to $|\mathbf{v}| = 0$. The largest value of n in $1/\alpha^n$ is determined by the highest harmonic of Legendre polynomials, so that the error grows with the number of requested Legendre harmonics. The tests have shown that for $T_e \sim 5$ keV, the value of *mx* should be limited by 3. This imposes a limitation for the fully relativistic operator, which can be eliminated in future by combining the fully-relativistic operator with quasi-relativistic for the low- $|\mathbf{v}|$ range. The quasi-relativistic operator does not have $1/|\mathbf{v}|$ divergent terms because of the much less complicated structure of the kernel, as given by Eq. (4). Although the $M_l(\mathbf{v})$ -integral given by Eq. (15) can be divergent for high l and small \mathbf{v} , it enters the expressions for g_a and h_a potentials with the weighting factor u^{l+2} , so that the whole term is not divergent. Similar condition holds for all terms incorporated into g_a and h_a potentials of the quasi-relativistic formulation.

At present, the situation with divergent terms in fully relativistic operator is improved by re-writing expressions for derivatives of γ^m/α^n and $\gamma^m \sinh^{-1}(\alpha)/\alpha^n$ in order to increase accuracy (by collecting all terms with the same power of α), and also by modifying subroutine *cfpleg* which evaluates Legendre coefficients for the distribution function. As an option, it zeroes coefficients $V_l^b(\mathbf{v})$ with $l > 3$ at small \mathbf{v} , while retaining them at large \mathbf{v} . With these modifications, the fully relativistic operator can be used with *mx* up to 5, although it is recommended not to exceed *mx* = 3.

All tests here are done with *mx* = 3 Legendre harmonics. The tests with *relativ* = ‘enabled’ (quasi-relativistic operator) show that increasing *mx* to 5 does not add noticeable features to the final distribution function in all three types of tests performed in this study.

IV. BENCHMARKING

1. Conductivity test

The conductivity of plasma in relativistic limit has been calculated in [8] using generating functions $y_{l[k]*}$ and $j_{l[k]*}$ as described at the end of Section I. Imposing a weak electric field along the magnetic field results in a first order correction to initially Maxwellian electron distribution function. The steady state is achieved due to collisions of electrons with background electrons and ions. This approach is implemented in the ADJ code which is used as a reference point for CQL3D calculations of conductivity.

For benchmarking purposes of the code, the plasma is considered to be uniform in density and temperature. The main parameters in the *cqlinput* namelist are given below and in Table I.

Pitch-angle (θ) grid: *iy* = 200; Momentum (\mathbf{v}) grid: *jx* = 330;

Legendre harmonics’ number: *mx* = 3;

Time step: see Table I; Number of time steps: $nstop = 16$;
‘Seed’ electric field: $elecfl d(0) = 9.17e-7$, $elecfl d(1) = 9.17e-7$ (flat radial profile);
Largest energy on the (v, θ) -grid: $enorm = 39.1389 * T_e [\text{keV}]$
($enorm = 20,000$ keV for $T_e = 511$ keV);
Boundary conditions: $lbdry(1)='fixed'$, $lbdry0='disabled'$;
Density of species ($reden(*,*)$): $n_e = n_i = 10^{14} \text{ cm}^{-3}$, flat profile; n_i is adjusted for $Z_i > 1$.
Temperature: see Table I; ion temperature is equal to electron temperature; flat profiles.

TABLE I. Main parameters for benchmarking.

T_e (keV)	$enorm$ (keV)	τ_{ee} (sec)	τ_{ii} (sec)	Tested time step, dtr (sec)	dtr/τ_{ee}
5.11	200	1.8592e-5	3.0775e-3	0.2 – 50	1e4 – 3e6
51.1	2,000	5.8794e-4	9.7318e-2	6 – 50	1e4 – 1e5
511.	20,000	1.8592e-2	3.0775	50 – 200	3e3 – 1e4
5,110.	200,000	0.58794	97.318	50 – 6,000	1e2 – 1e4
51,100.	2,000,000	18.592	3.0775e+03	20,000 – 200,000	1e3 – 1e4

In the first round of tests, conductivity is calculated for the near-axis region of plasma. The results from CQL3D for $\varepsilon = r/R = 1e-6$ are compared with data from Braams-Karney [8] which correspond to $\varepsilon = 0$. Five groups of runs with different plasma temperatures are performed. For each temperature value, the maximum energy on the grid is adjusted to maintain $enorm = 39.1389 * T_e [\text{keV}]$. If $enorm$ is set too large, the resolution in velocity grid at $v \sim v_{th}$ is reduced. On the other side, if $enorm$ is too small, the effects of the tail formation in the distribution function can be missed. The value of $enorm$ is related to the largest momentum-per-rest-mass (v_{norm}) on the grid by $enorm/mc^2 = \gamma_{norm} - 1$, where $\gamma_{norm} = (1 + (v_{norm}/c)^2)^{1/2}$. As the relativistic Maxwellian distribution function is proportional to

$$f_m(v) \propto \exp\left(-\frac{(\gamma - 1)mc^2}{T}\right),$$

it is clear that the ratio $enorm/T$ defines the drop factor of the distribution function at $v = v_{norm}$,

$$\frac{f_m(v_{norm})}{f_m(0)} = \exp\left(-\frac{enorm}{T}\right),$$

which equals to $\exp(-39.1389) \approx 1.e-17$ in this case.

The time step dtr was selected to be large enough that the distribution function can reach a steady state in a small number of iterations. The fully implicit method of integration allows setting dtr to a nonphysically large value for implicit steady state calculations. The values of dtr specified in Table I allowed achieving steady state in 16 time steps.

The option chosen for the boundary conditions implies that the distribution is held constant at $v = 0$ during "time" advancement. If a tail is formed in the distribution, the total density will grow. An alternative option is to set $lbdry(1)='conserv'$, which implies the conservation of the total density, but not the value of $f(0)$. In most tests on conductivity, the results obtained with either boundary condition do not significantly differ. (It should be mentioned, though, that in runs at $T_e \sim 5$ keV, the option $lbdry(1)='conserv'$ results in a sudden jump of conductivity, if the fully-relativistic operator is used. The problem is removed by reducing mx to 2.)

The calculated values of conductivities at the near-axis region of plasma ($\varepsilon = r/R = 1e-6$) are shown in Table II; ion charge is $Z_i = 1$ in these runs. In the case of the non-relativistic collision operator (*relativ='disabled'*), the conductivity does not show any significant dependence on T_e . In the case of $T_e = 51.1$ MeV, the electric field is reduced to *elecfl* $d = 9.17e-8$, otherwise a strong deformation is developed in the distribution due to run-away electrons.

TABLE II. Normalized conductivities for effective ion charge $Z_{eff} = 1$. The conductivities are

normalized to $\sigma_n = \frac{1}{\sqrt{m_e} 4\pi e^2 \ln \Lambda} \frac{(k_B T_e)^{3/2}}{Z_{eff}}$ [cgs units].

T_e (keV)	<i>elecfl</i> <i>d</i> (cgs)	CQL3D <i>relativ='disabled'</i>	CQL3D <i>relativ='enabled'</i>	CQL3D <i>relativ='fully'</i>	Braams- Karney [8]
5.11	9.17e-7	7.40313	7.26529	7.27454	7.27359
51.1	9.17e-7	7.40313	6.29477	6.18808	6.20946
511.	9.17e-7	7.40371	3.21786	3.11544	3.13472
5,110.	9.17e-7	7.46231	1.04061	1.00528	1.02875
51,100.	9.17e-7	24.9037 (run-away <i>e</i>)	0.33281	0.29501	0.32528
51,100.	9.17e-8	7.46249	0.28052	0.27409	0.32528

In the second round of tests, the conductivity is calculated for different radial points (ε); results from CQL3D are compared with that obtained from the ADJ code. The results are summarized in Figs. (1-4). Black dots (connected) correspond to normalized conductivity calculated with the ADJ code. The pitch-angle grid size, momentum grid size, and the factor of *enorm/T* in ADJ runs are set equal to those in CQL3D runs. The number of Legendre harmonics is also set to 3 in ADJ runs, although changing it to 5 affects only the 5th-6th digit in value of conductivity. For CQL3D runs displayed in Figs. (1-4), the time step is set according to $dtr = 10^4 \tau_{ee}$. The value of the electric field in all runs is set to *elecfl* $d = 9.17e-8$; for such field the distortion of the distribution function remains negligible even for the high temperature of $T_e = 51.1$ MeV. In runs with $Z_i = 5$, the density of ions is reduced by 5.

Both quasi-relativistic and fully-relativistic collision operators in CQL3D show good agreement with each other and with the ADJ code. For $T_e/m_e c^2 \geq 1$, the fully relativistic operator in CQL3D yields a better match with the ADJ code. For $Z_i = 5$, $T_e/m_e c^2 = 100$, both operators in CQL3D give a somewhat lower value of conductivity than in ADJ, but agree perfectly with each other (bottom curve in Fig. 2).

It is surprising to see that even at a very high temperature, $T_e = 51.1$ MeV = $100 m_e c^2$, the quasi-relativistic operator yields conductivity values close to those obtained with the fully relativistic operator. A possible explanation is that the value of conductivity is determined mostly by collisions of electrons with ions, even for $Z_i = 1$. In the first-order approximation, the difference between fully-relativistic and non-relativistic kernels is [6]

$$|\mathbf{U}_r| - |\mathbf{U}_{nr}| \approx \beta^2 \beta'^2 |\mathbf{U}_{nr}|,$$

where $\beta = u/c$, with u being the velocity (not momentum per rest mass).

For 51.1 MeV electrons,

$$\beta = \frac{v_{th}/c}{\sqrt{1 + (v_{th}/c)^2}} = \left(\frac{T_e/m_e c^2}{1 + T_e/m_e c^2} \right)^{1/2},$$

so that $\beta^2 = 100/101 = 0.99$.

For 51.1 MeV deuterium ions, however,

$$\beta'^2 = (100/3670) / (1 + 100/3670) = 0.0265.$$

Hence, $|\mathbf{U}_r| - |\mathbf{U}_{nr}| \approx 0.026|\mathbf{U}_{nr}|$ in our case.

For verification, a test is performed with artificially light ions, $m_i = 2m_e$. The results are given in Table III, third line. The results for “normal” deuterium ions are repeated in the second line, for comparison. Also, results are shown for artificially heavy ions. It is seen that the fully relativistic operator yields a 33% smaller conductivity than the quasi-relativistic operator, when all interacting species are highly relativistic ($\beta^2 > 0.98$). It should be noted that in Braams-Karney calculations [8] given in Table II, and in the ADJ code, the ions are considered infinitely massive.

TABLE III. Normalized conductivities for different ion masses.

Plasma parameters: $T_e = T_i = 51.1$ MeV, $Z_i = 1$, $elecfl d = 9.17e-8$, $\varepsilon = 1e-6$.

m_i	CQL3D <i>relativ='enabled'</i>	CQL3D <i>relativ='fully'</i>	difference
3.3433e-21 g (2000 m_H)	0.3091	0.3019	2.3 %
3.3433e-24 g (= 2 m_H)	0.2805	0.2741	2.3 %
1.8219e-27 g (= 2 m_e)	0.3134	0.2093	33 %

As mentioned above, for $T_e = 51.1$ MeV and $elecfl d = 9.17e-7$, the distribution function becomes visibly distorted. This is the only case when the quasi-relativistic and fully relativistic operators yield visibly different, although not significantly different, distribution functions. The results are displayed in Figs. (5-12). For comparison, the results from *relativ='disabled'* run (non-relativistic operator) are also shown in Figs. (13-16), although they don't have much physical meaning at such temperature. Note that v_{norm} is different in non-relativistic case, since it is determined from $enorm = mv_{norm}^2/2$; thus, $v_{norm}/v_{th} = 391$ in Figs. (5-12), but $v_{norm}/v_{th} = 8.85$ in Figs. (13-16), where $v_{th} = (T_e/m_e)^{1/2}$.

2. LH test

The lower hybrid heating/current drive scenario provides a good opportunity for testing relativistic operators, because it involves interaction of high-energy electrons with (possibly) relativistic bulk electrons. Two cases are considered in this part: $T_e = 511$ keV ($T_e/m_e c^2 = 1$), and $T_e = 30$ keV, which is a realistic temperature for ITER.

For tests, a simplified LH model is considered, for a single flux surface with analytical equilibrium magnetic field. The wave parameters are specified in *cqlinput*, with *vlhmod='enabled'*. Parameters *vparmin* and *vparmax* allow setting the range of $u_{||}/c$ (velocity; not momentum per rest mass) where the wave interacts with the distribution. For the $T_e = 511$ keV run, these parameters are set to

$$vparmin = u_{||min}/c = 0.94107937416983, \text{ corresponding to } 1 \text{ MeV,}$$

$$vparmax = u_{||max}/c = 0.99994882620149, \text{ corresponding to } 50 \text{ MeV.}$$

The magnitude of the RF diffusion coefficient in units of v_{th}^2 / τ_{ei} is set to $dlndau = 200$.

Other main parameters:

Pitch-angle (θ) grid: $iy = 200$; Momentum (v) grid: $jx = 200$;
Legendre harmonics' number: $mx = 3$;
Time step: $dtr = 200$; Number of time steps: $nstop = 8$;
Largest energy on the (v, θ)-grid: $enorm = 50,000$ keV;
Boundary conditions: $lbdry(1)='conserv'$, $lbdry0='enabled'$;
Density of species ($reden(*,*)$): $n_e = n_i = 10^{13}$ cm⁻³.

The results obtained with quasi-relativistic and fully relativistic operators are compared in Figs. (17-21). The fully relativistic operator yields a less extended tail in distribution. As a result, the driven current is about 25% smaller, as seen in Figs. (20-21).

In the second case, $T_e = 30$ keV, the range of resonant $u_{||}/c$ is set to
 $vparmin = 0.866026$, corresponding to 511 keV,
 $vparmax = 0.995692$, corresponding to 5 MeV.

The magnitude of the RF diffusion coefficient is set to $dlndau = 40$. The largest energy is adjusted to $enorm = 5,000$ keV, and the time step is reduced to $dtr = 5$; all other parameters are kept the same as in the previous case. The results obtained with the two relativistic operators are compared in Figs. (22-26). The current is small here, because the resonant region is shifted to the high energy relativistic range of $u_{||}/c$. The difference is very small; the current calculated with fully relativistic operator is only 4.8% smaller than with the quasi-relativistic operator. Even though the electron tail is in the relativistic MeV region, the bulk electrons are not ($\beta'^2 \approx 0.11$), which explains why the quasi-relativistic operator works well in such a case.

3. ECH test

In electron cyclotron heating, a high-energy tail can be formed in electron distribution. Here, a typical DIID ECH scenario is examined with quasi-relativistic and fully relativistic operators. The wave parameters are set to (with $vlfmod = 'enabled'$):

$vlfharm1 = 2.$, harmonic number;
 $vlfnpvar = '1/R'$, sets 1/R variation to parallel refractive index;
 $vlfdnorm(1) = 10000.$, strength of QL diffusion coefficient, normalized to v_{th}^2 / τ_{ei} ;
 $vlfreq(1) = 110.e9$, frequency (Hz);
 $vlfnp(1) = 0.5$, parallel refractive index at minimum B ;
 $vlfndp(1) = 0.2$, width of parallel refractive index;
 $vlfddnp(1) = 0.1$, additional region of par. refr. index, in which the QL coeff. tapers to 0;
 $vlfnp(1) = 0.5$, perpendicular refractive index;
 $vlfep(1) = (0.5,0.)$, complex $E_+ / |E|$ polarization;
 $vlfemin = (0.5,0.)$, complex $E_- / |E|$ polarizaion.

Other main parameters:

Pitch-angle (θ) grid: $iy = 200$; Momentum (v) grid: $jx = 200$;
Legendre harmonics' number: $mx = 3$;
Time step: $dtr = 1$; Number of time steps: $nstop = 4$;
Largest energy on the (v, θ)-grid: $enorm = 700$ keV;
Boundary conditions: $lbdry(1)='fixed'$, $lbdry0='disabled'$;

Density of species (*reden(*,*)*): $n_e = n_i = 5 \times 10^{13} \text{ cm}^{-3}$.
 $T_e = 6 \text{ keV}$, $T_i = 1 \text{ keV}$.

The results are presented in Figs. (27-30). The quasi-relativistic and fully relativistic operators yield almost indistinguishable results in this case.

V. SUMMARY

The fully relativistic collision operator in CQL3D is shown to be operational. The numerical instability at low- v range, which is caused by $1/v$ divergent terms, can be avoided by limiting the number of Legendre harmonics by 3. This problem can be addressed in future by using quasi-relativistic approximation at lower v . The tests have shown close comparison (maximum difference 3.5% up to 51 MeV, <1.7% below 51 keV) in calculated conductivity values obtained with the fully-relativistic and quasi-relativistic operators. In fusion energy applications, the quasi-relativistic operator can be used instead of the fully relativistic operator, because usually the relativistic particles either interact with non-relativistic ions (conductivity calculations), or relativistic electrons in the tail of distribution interact with bulk non-relativistic electrons. The only exception, when the results from the quasi and fully relativistic operators show a noticeable difference, is the LH case with $T_e/m_e c^2 \approx 1$ or higher. In comparisons of the conductivity calculated with the CQL3D fully relativistic operator and the ADJ self-adjoint code, CQL3D gives <0.6% (less) up to 511 keV, 2.2% at 5 MeV, and 16% at 51 MeV.

ACKNOWLEDGEMENTS

This work was supported by USDOE Contract DE-FC02-ER54698 through General Atomics, Fusion Division. The authors are grateful to Dr. Ron Prater for appreciating the necessity of this benchmarking effort, and for encouragement.

REFERENCES

- [1] L.D. Landau Phys. Z. Sowjetunion **10**, 154 (1936).
- [2] S.T. Beliaev and G.I. Budker, Dokl. Akad. Nauk SSSR **107**, 807 (1956) [Sov. Phys. Dokl. **1**, 218 (1957)].
- [3] M.N. Rosenbluth, W.M. MacDonald, and D.L. Judd, Phys. Rev. **107**, 1 (1957).
- [4] B.A. Trubnikov, Sov. Phys. JETP **7**, 926 (1958).
- [5] J. Killeen, A.A. Mirin, and M.G. McCoy, *Modern Plasma Physics*, IAEA, Vienna, 1970.
- [6] M.R. Franz, *A Fully Relativistic Fokker-Planck Model of Multispecies Plasmas in a Nonuniform Magnetic Field*, Ph.D. Thesis, 1994.
- [7] B.J. Braams and C.F.F. Karney, Phys. Rev. Lett. **59**, 1817 (1987).
- [8] B.J. Braams and C.F.F. Karney, Phys. Fluids B **1**, 1355 (1989).

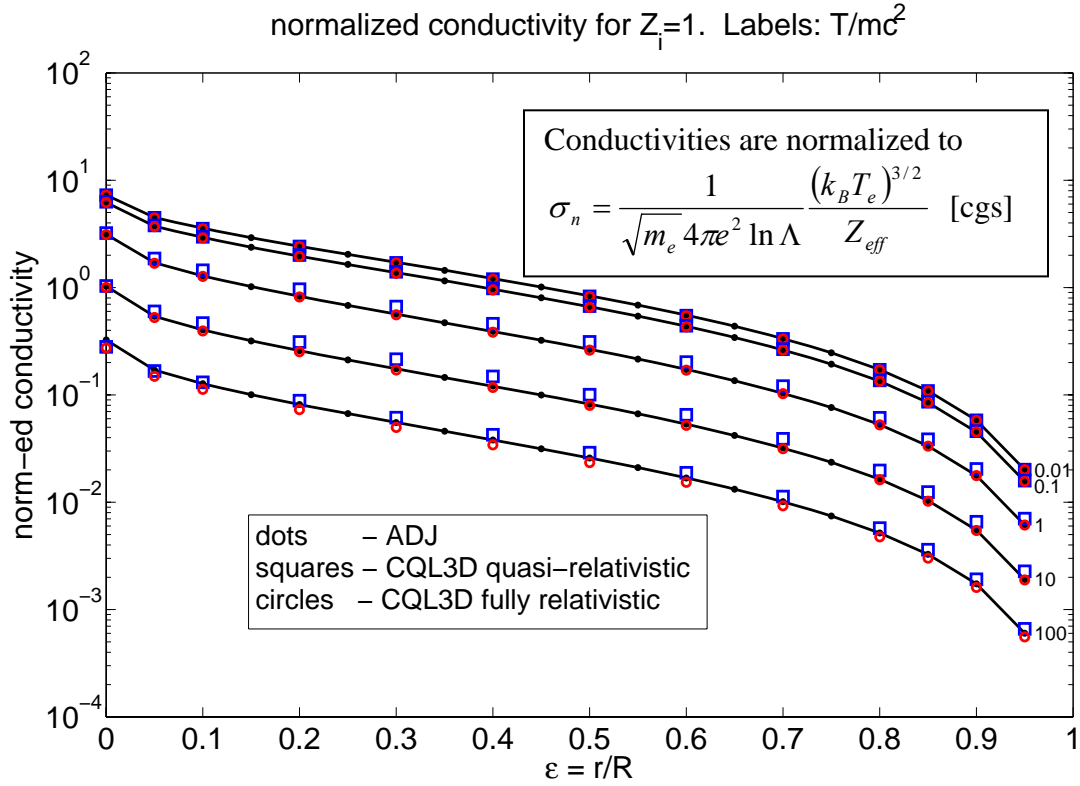


Fig.1. Conductivity test: Normalized conductivity as a function of inverse aspect ratio for different temperatures.

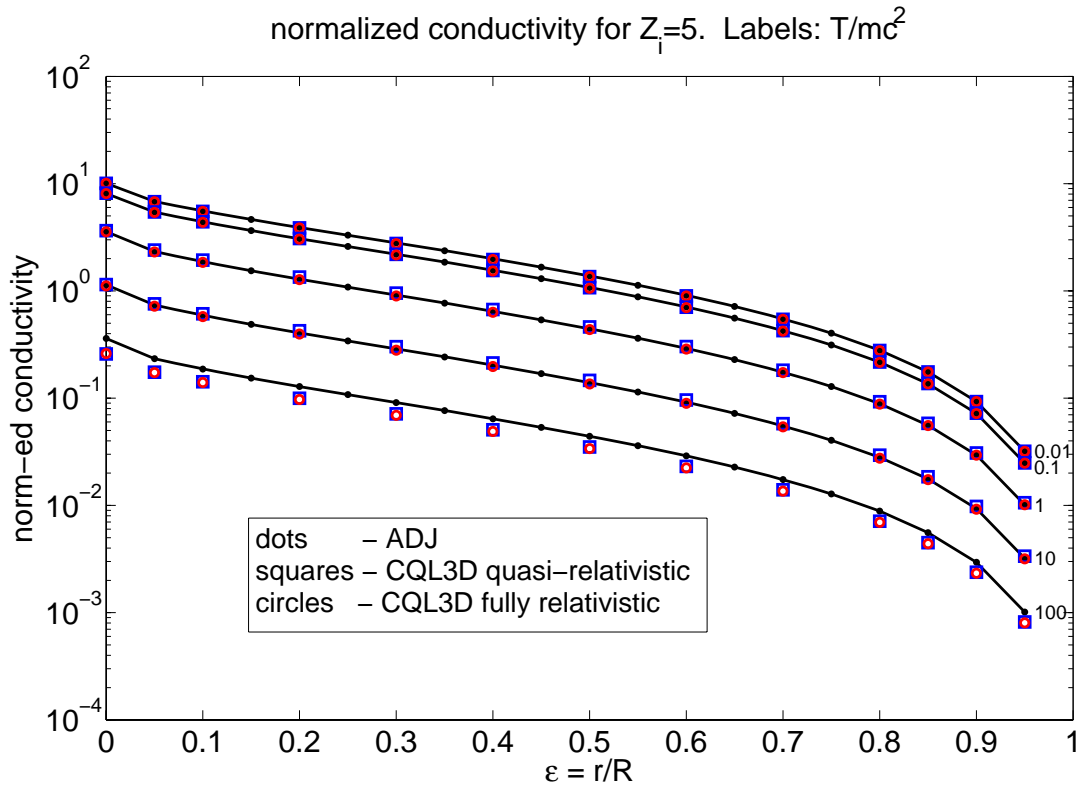


Fig.2. Conductivity test: Same as previous figure, but for $Z_i = 5$.

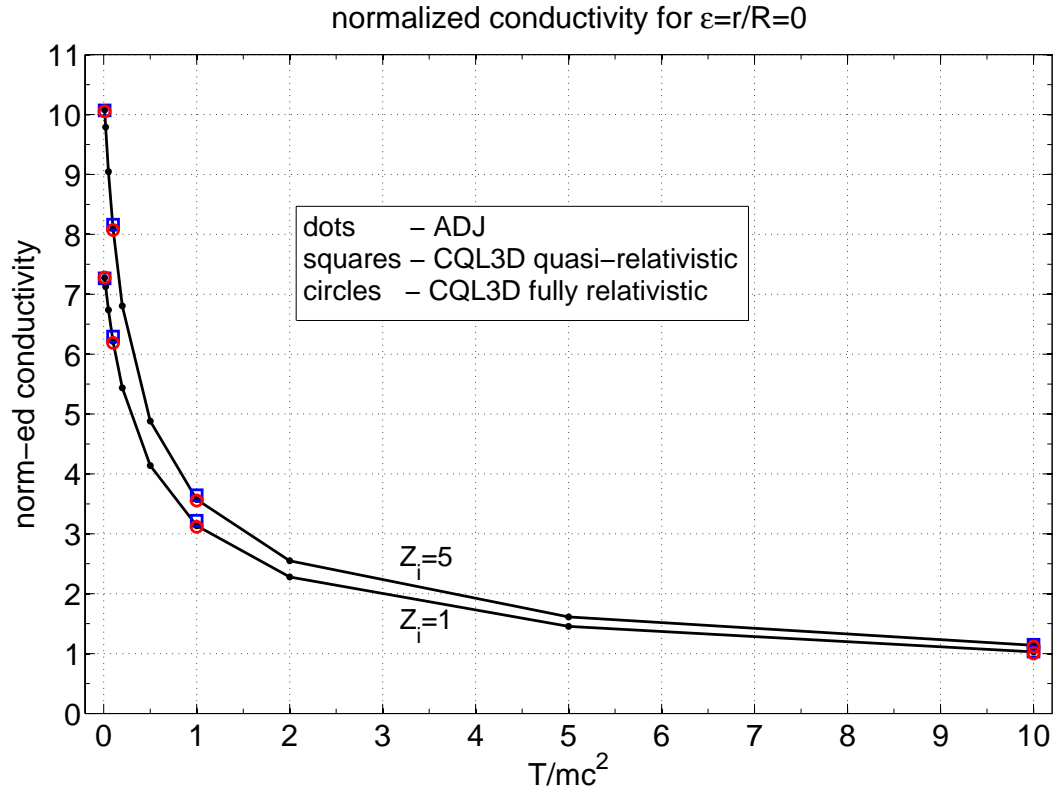


Fig.3. Conductivity test: Dependence of normalized conductivity on temperature in linear scale.

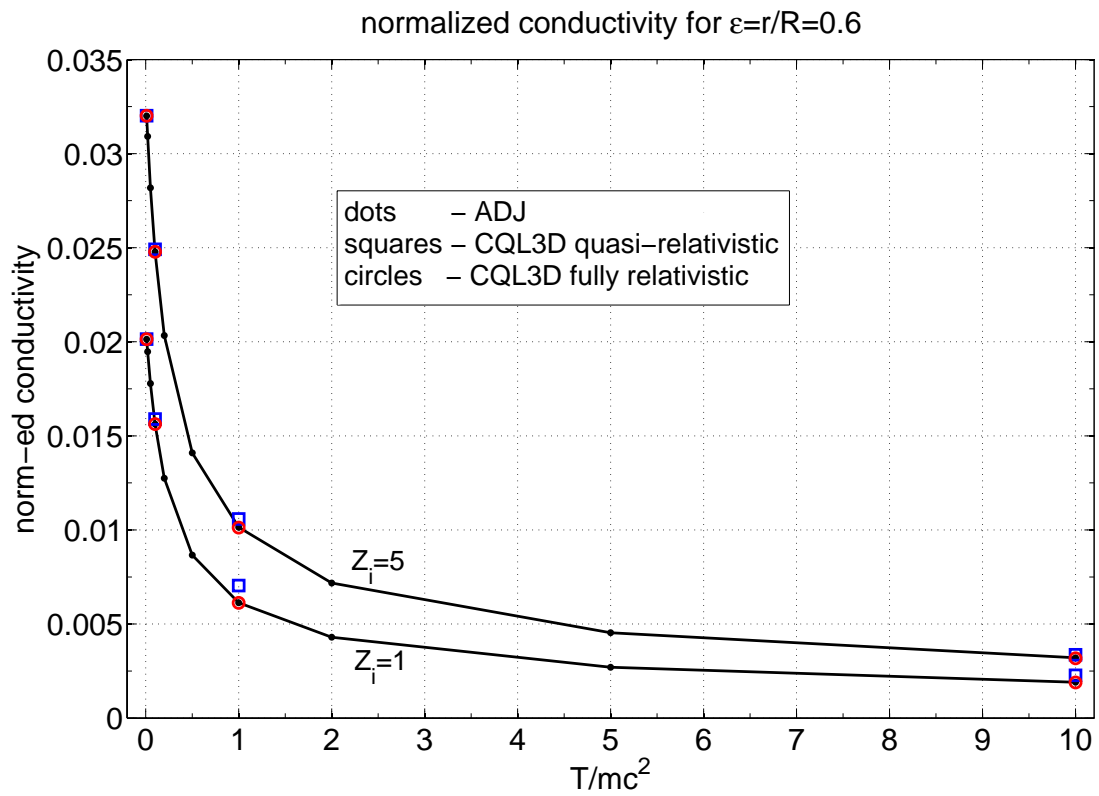


Fig.4. Conductivity test: Same as previous figure, but for $\epsilon = 0.6$.

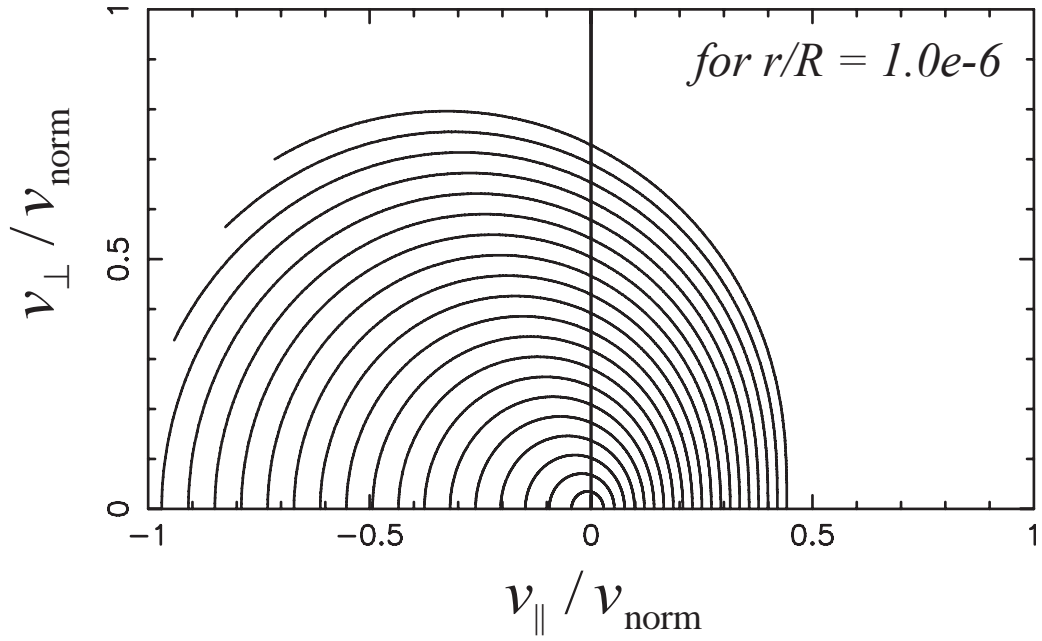


Fig.5. Conductivity test: Runaway electrons. Distribution function f_e for $T_e = 51.1$ MeV, *relative='enabled'* (quasi-relativistic operator), *elecfl=9.17e-7*.

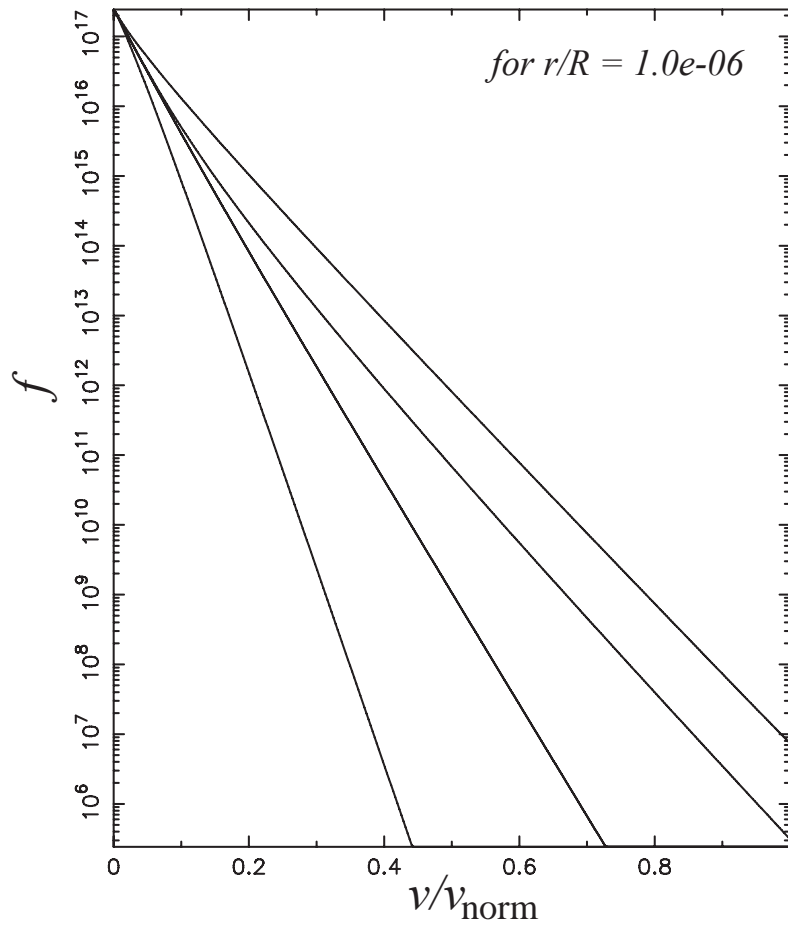


Fig.6. Cuts of f vs. v/v_{norm} at different pitch angles.

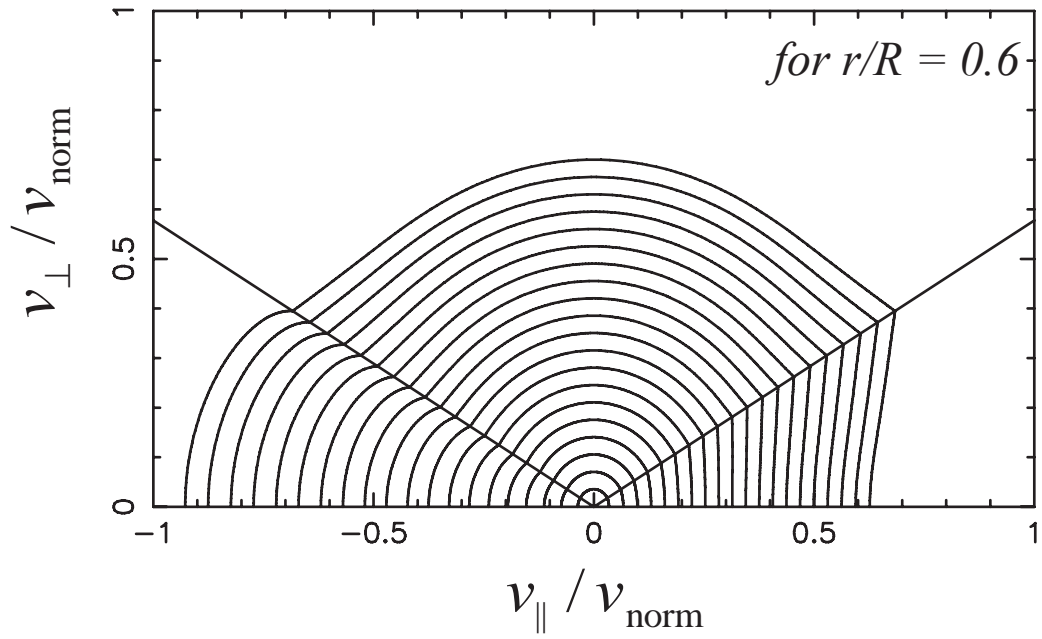


Fig.7. Conductivity test: Runaway electrons. Distribution function f_e for $T_e = 51.1$ MeV, *relative='enabled'* (quasi-relativistic operator), *elecfl=9.17e-7*.

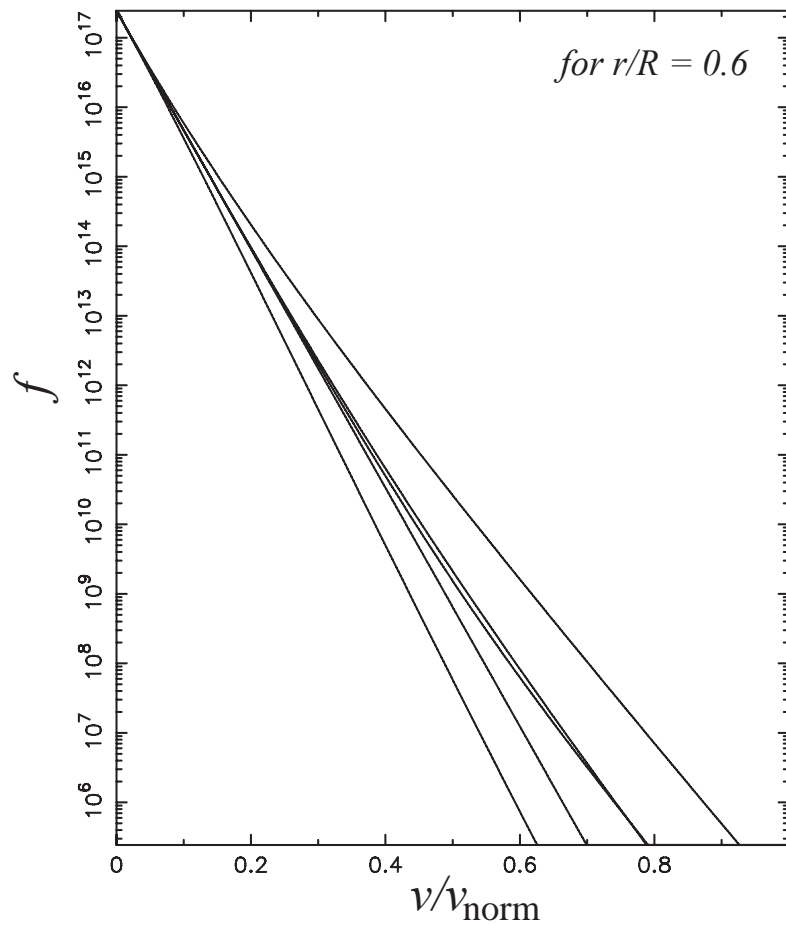


Fig.8. Cuts of f vs. v/v_{norm} at different pitch angles.

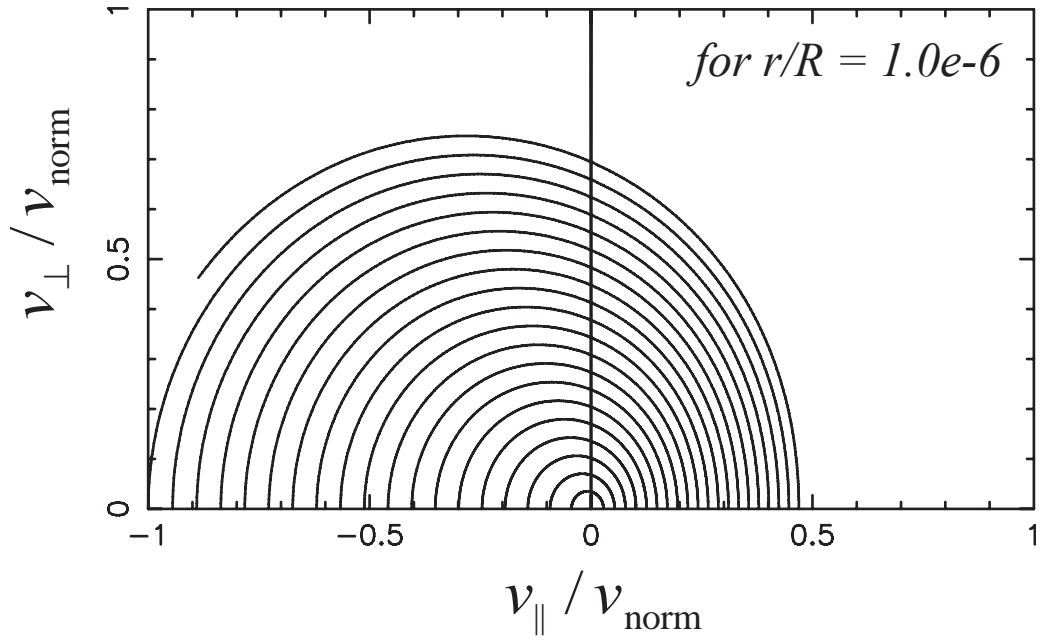


Fig.9. Conductivity test: Runaway electrons. Distribution function f_e for $T_e = 51.1$ MeV, *relative='fully'* (fully relativistic operator), *elecfl=9.17e-7*.

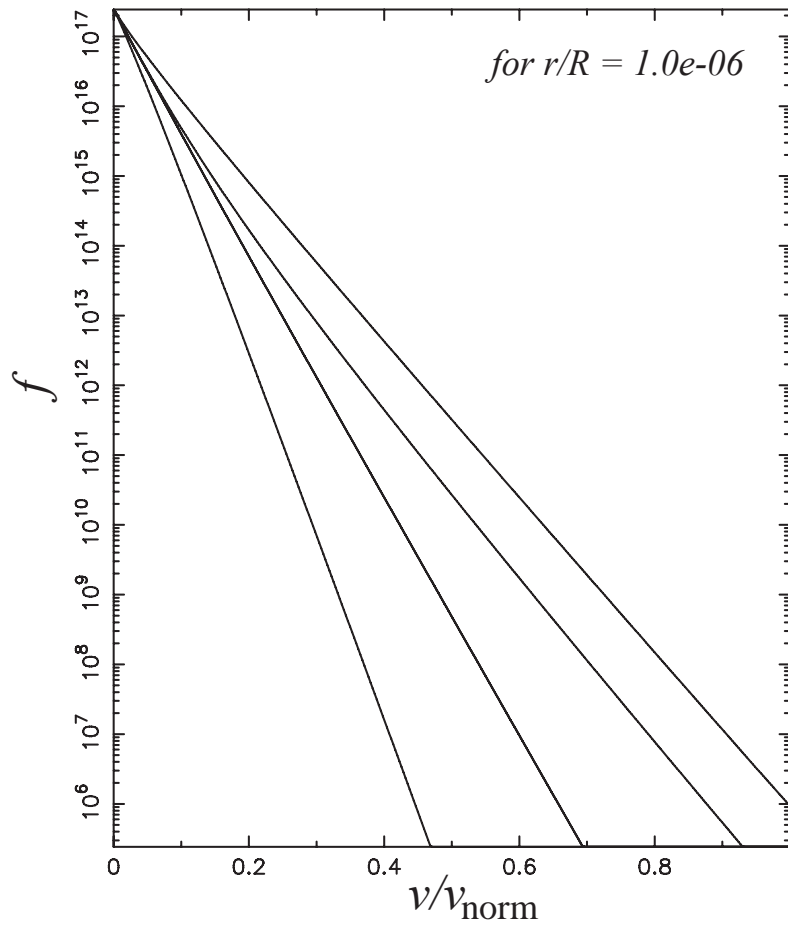


Fig.10. Cuts of f vs. v/v_{norm} at different pitch angles.

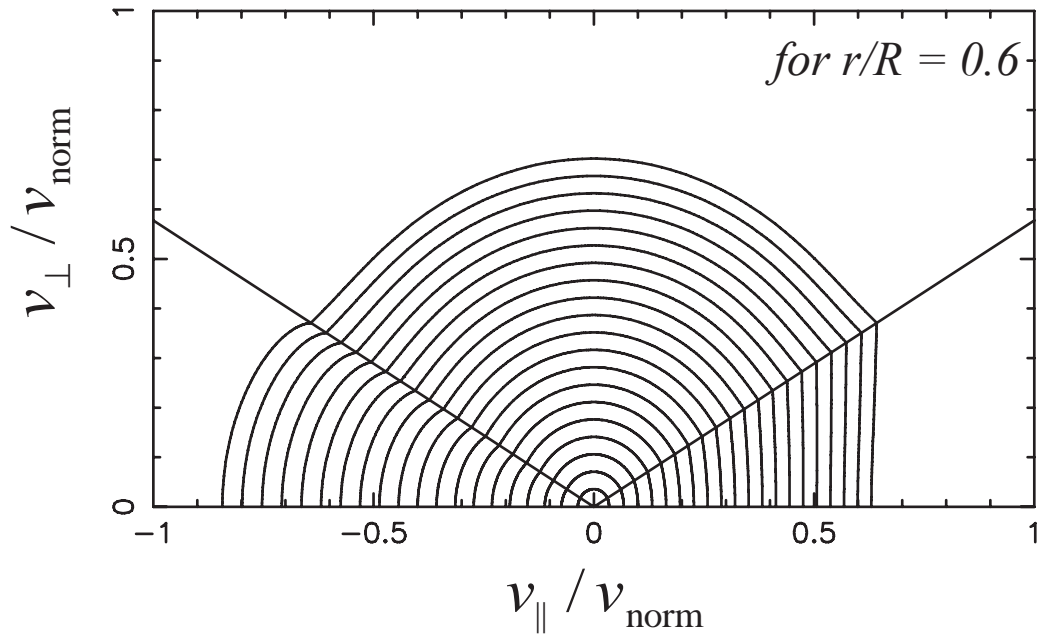


Fig.11. Conductivity test: Runaway electrons. Distribution function f_e for $T_e = 51.1$ MeV, *relative*=‘fully’ (fully relativistic operator), *elecfl* $d=9.17e-7$.

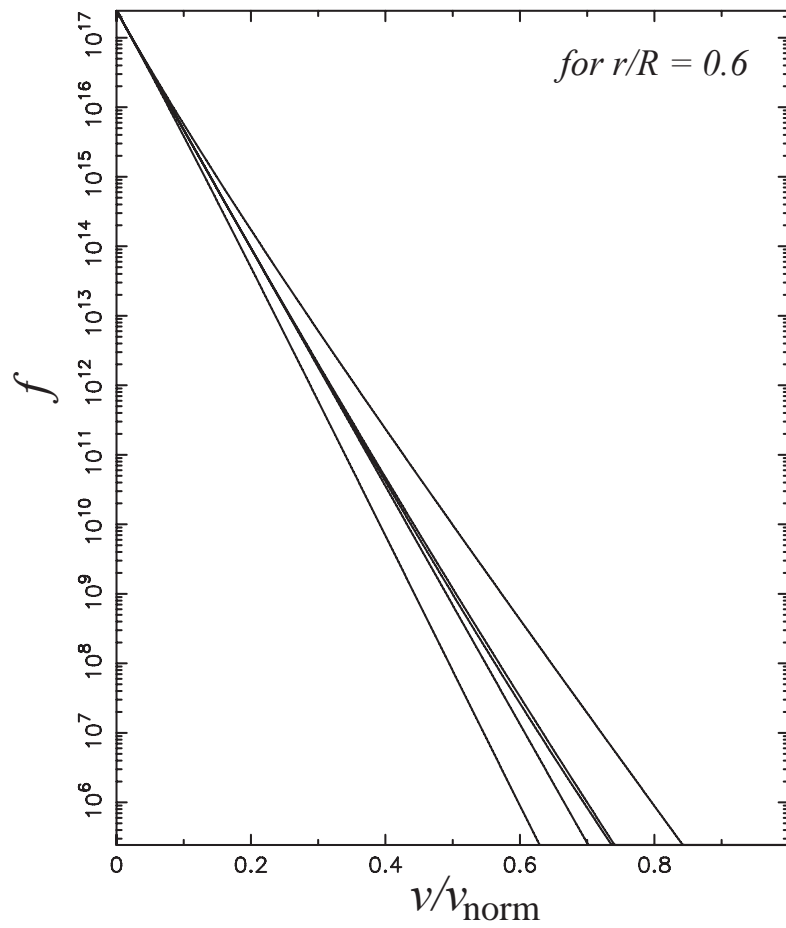


Fig.12. Cuts of f vs. v/v_{norm} at different pitch angles.

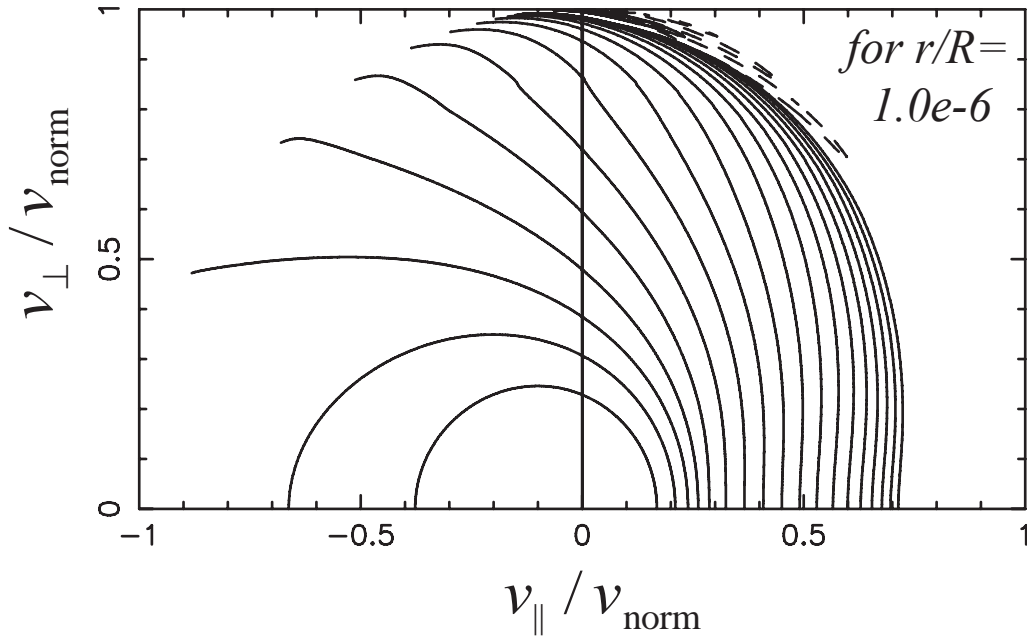


Fig.13. Conductivity test: Runaway electrons. Distribution function f_e for $T_e = 51.1$ MeV, *relative*='disabled' (non-relativistic operator), *elecfl* $d=9.17e-7$.

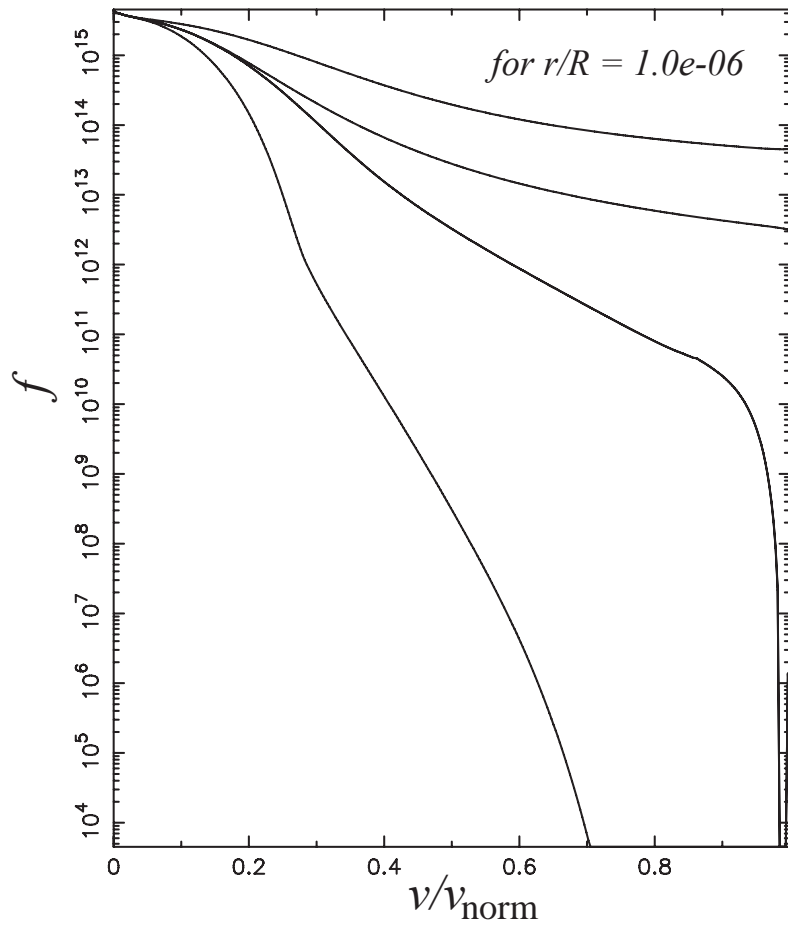


Fig.14. Cuts of f vs. v/v_{norm} at different pitch angles.

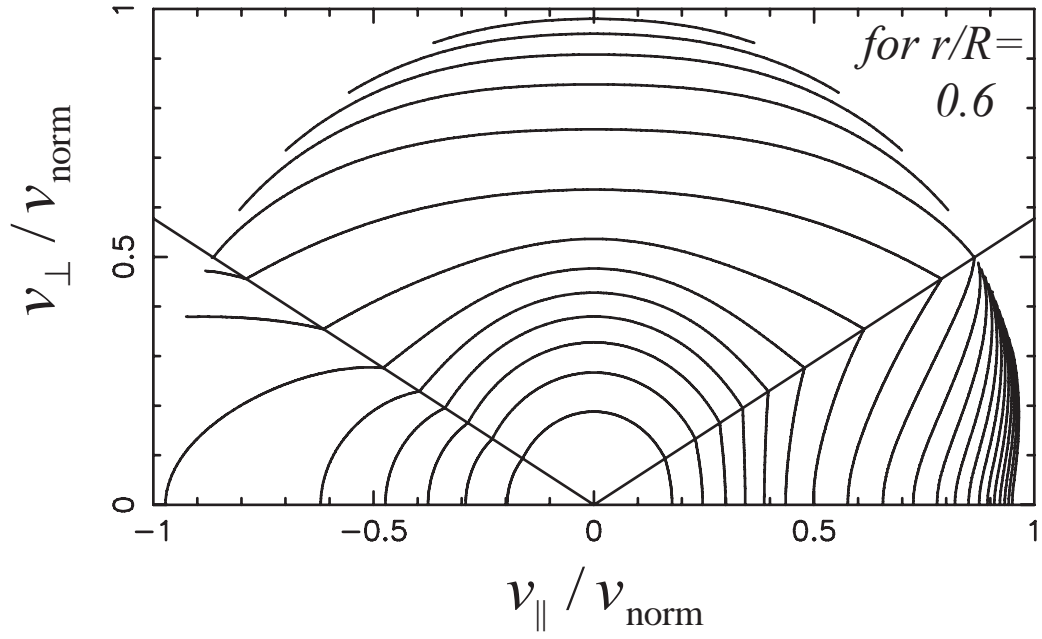


Fig.15. Conductivity test: Runaway electrons. Distribution function f_e for $T_e = 51.1$ MeV, *relative*='disabled' (non-relativistic operator), *elecfl* $d=9.17e-7$.

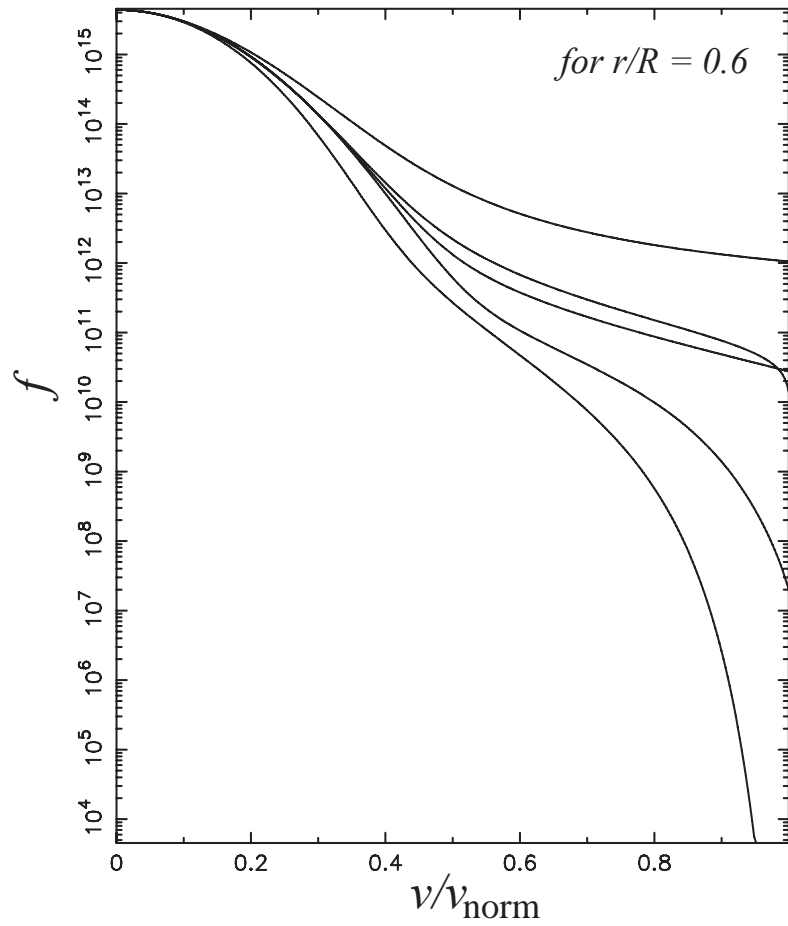


Fig.16. Cuts of f vs. v/v_{norm} at different pitch angles.

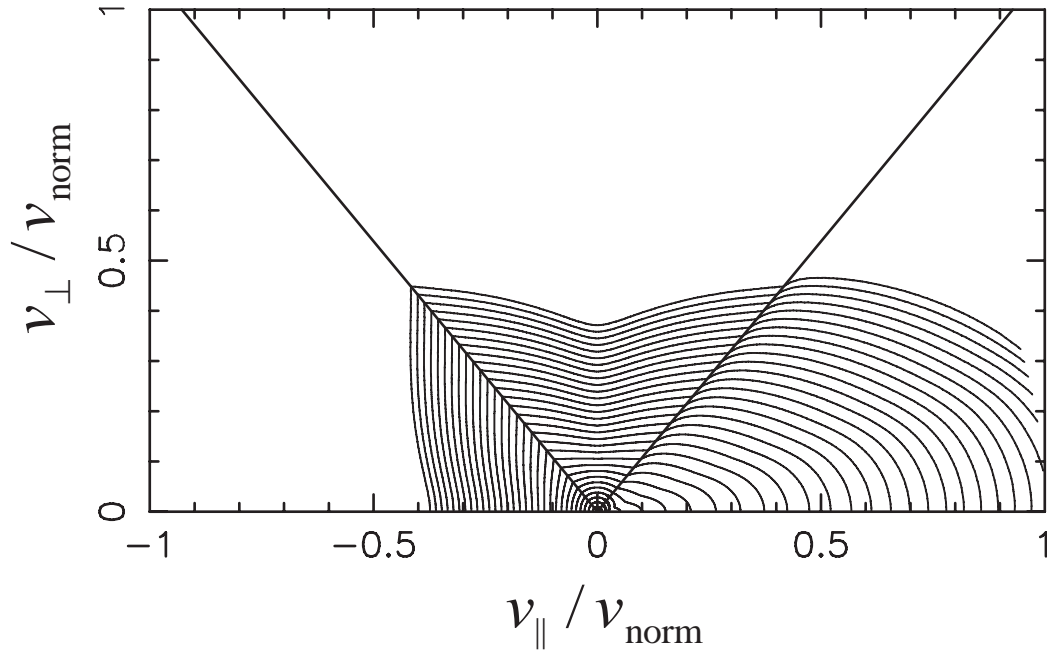


Fig. 17. LH-511keV test: Contour levels of distribution function in momentum space obtained with quasi-relativistic collision operator.

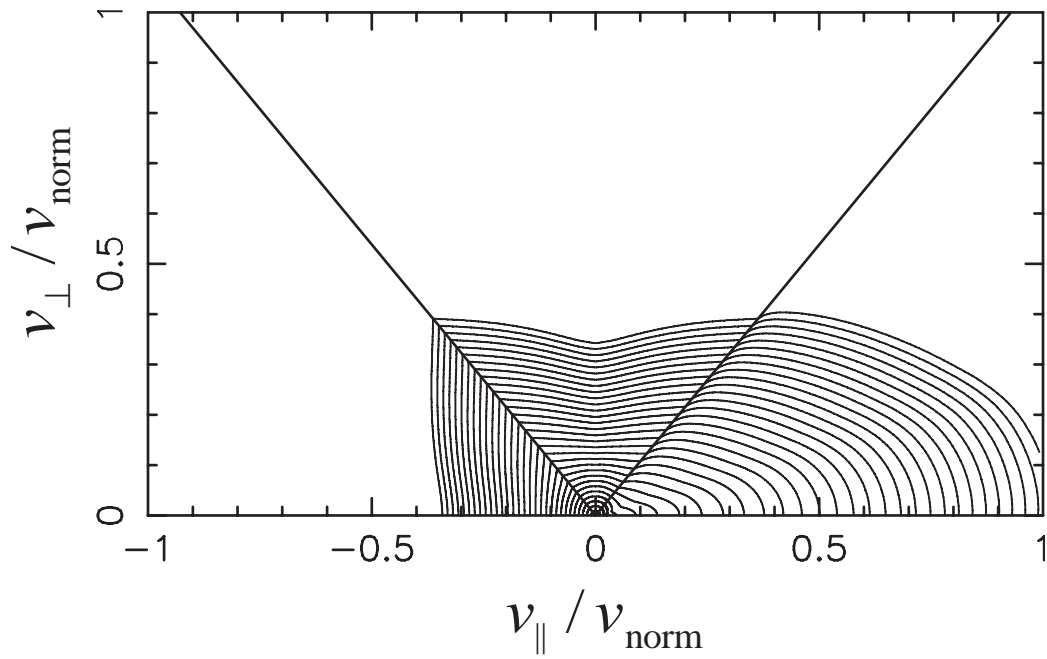


Fig. 18. LH-511keV test: Contour levels of distribution function in momentum space obtained with fully relativistic collision operator.

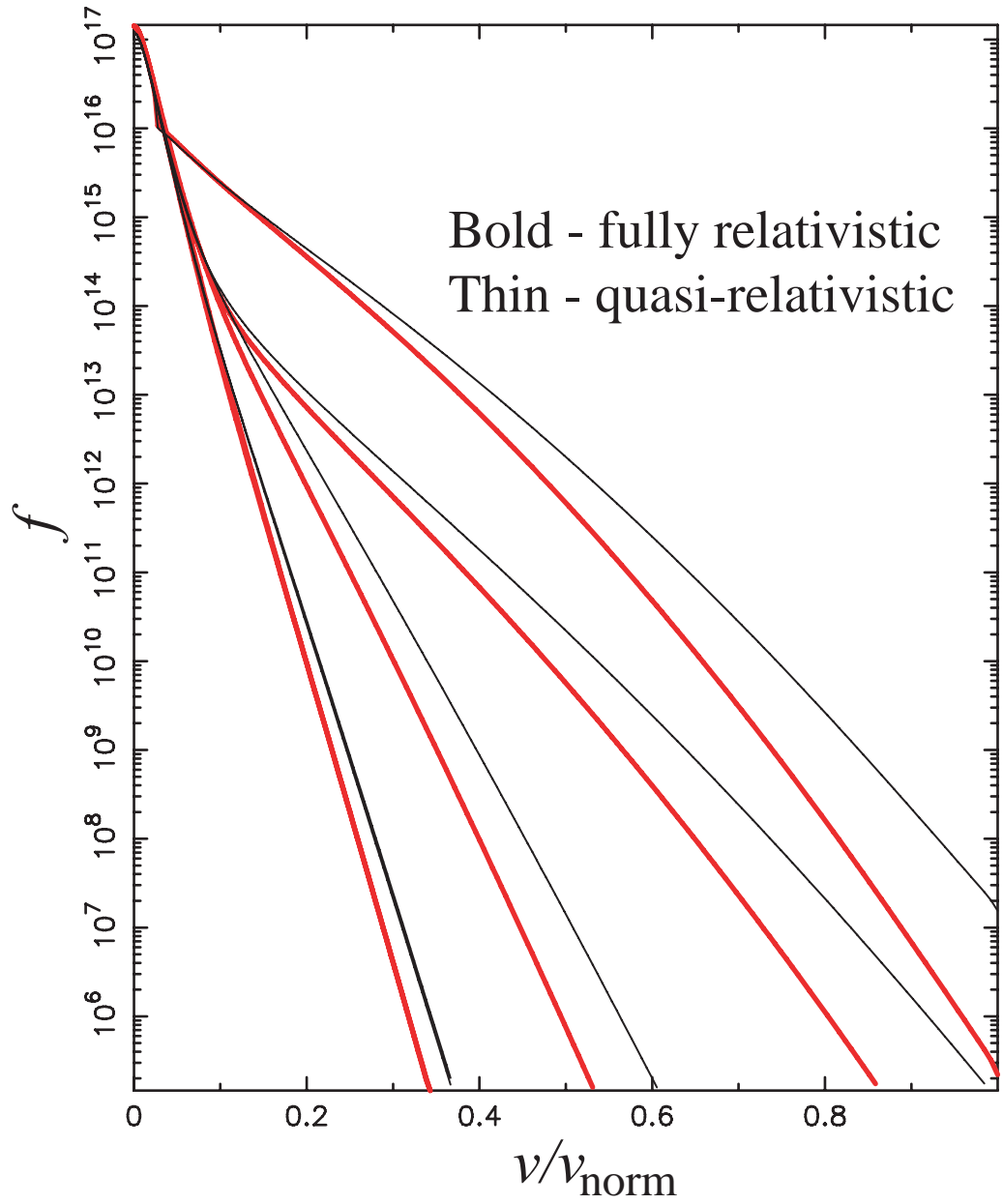


Fig. 19. LH-511keV test: Cuts of distribution function vs. v/v_{norm} at different pitch angles.

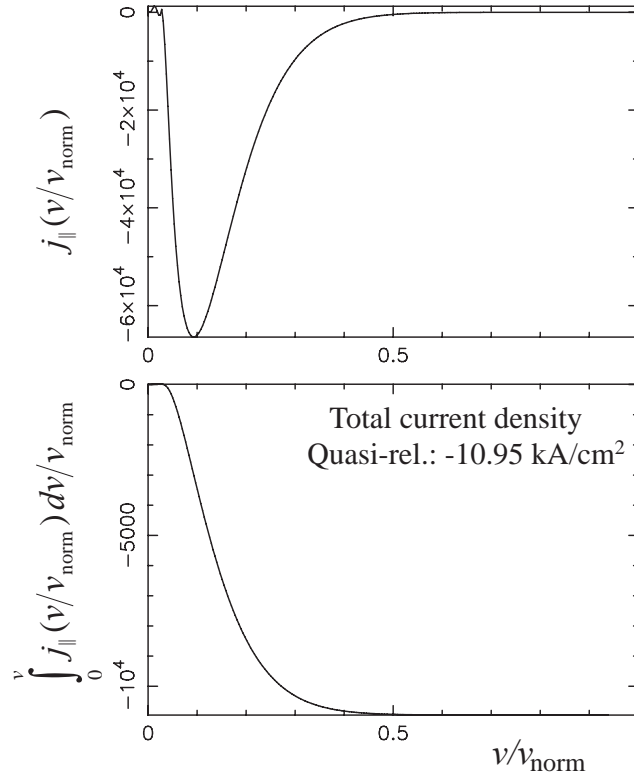


Fig. 20. LH-511keV test: Parallel current density as a function of normalized momentum, and corresponding cumulative value. Obtained with quasi-relativistic collision operator.

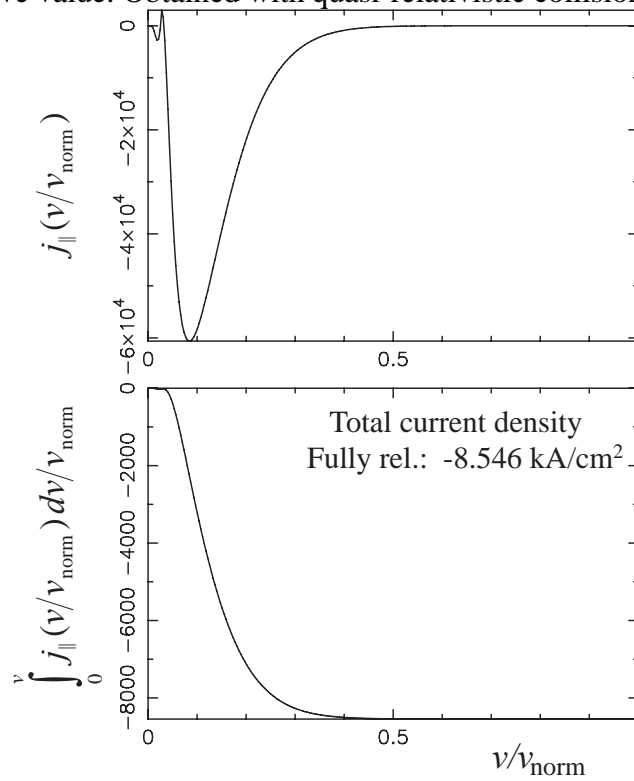


Fig. 21. LH-511keV test: Same as previous figure, but obtained with fully relativistic operator.

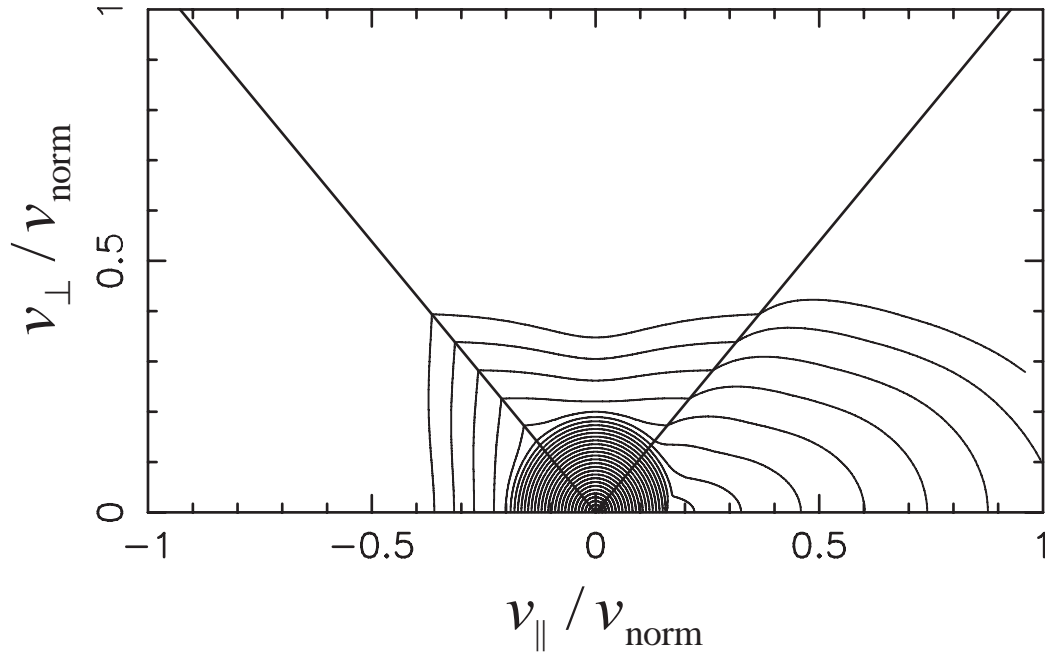


Fig. 22. LH-30keV test: Contour levels of distribution function in momentum space obtained with quasi-relativistic collision operator.

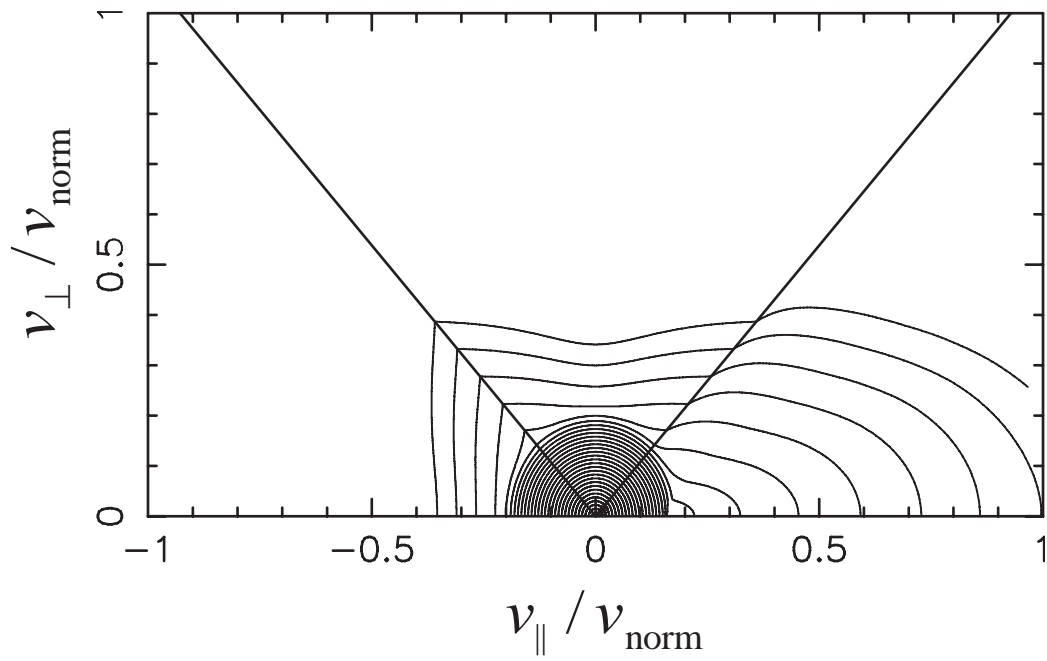


Fig. 23. LH-30keV test: Contour levels of distribution function in momentum space obtained with fully relativistic collision operator.

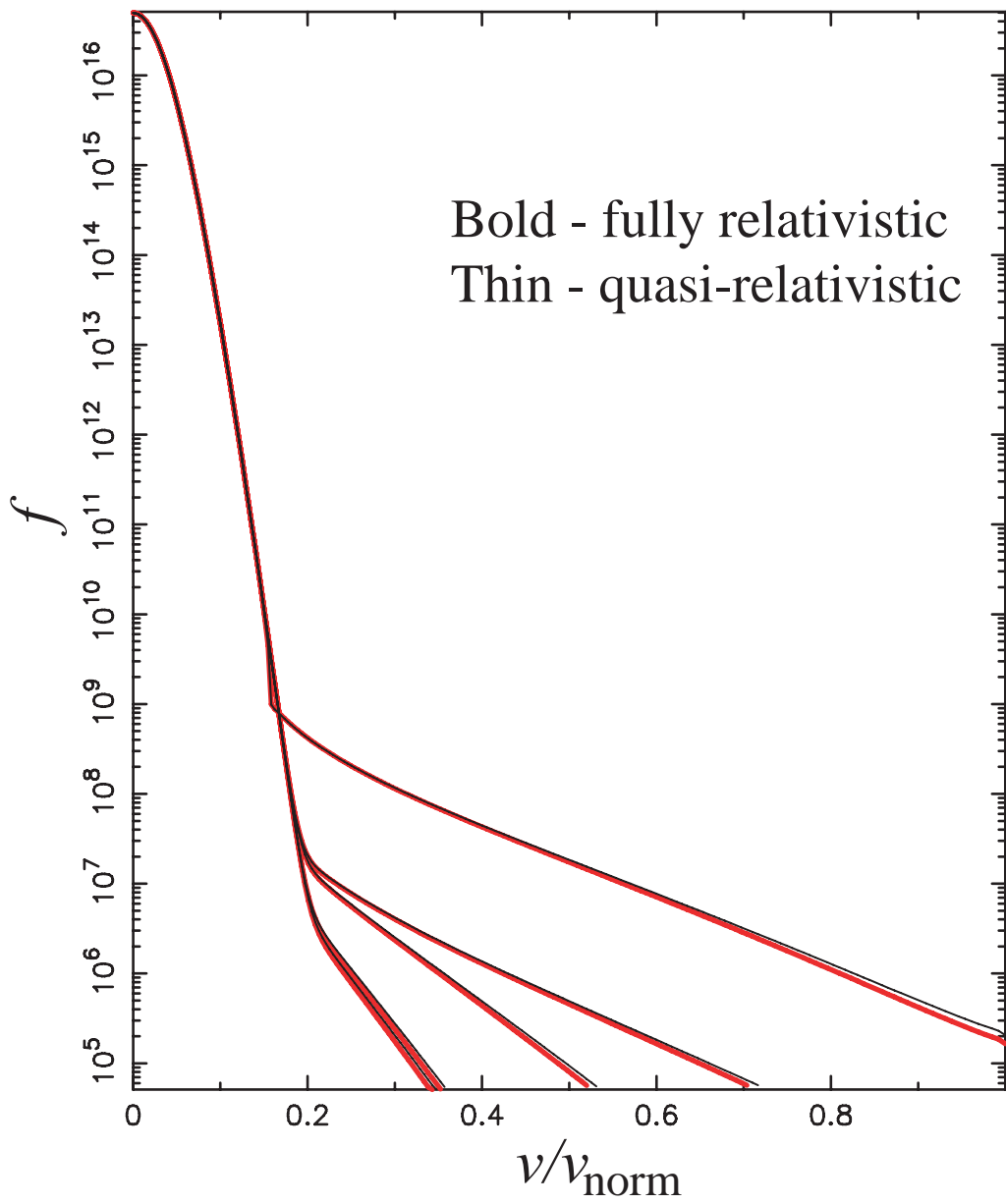


Fig. 24. LH-30keV test: Cuts of distribution function vs. v/v_{norm} at different pitch angles.

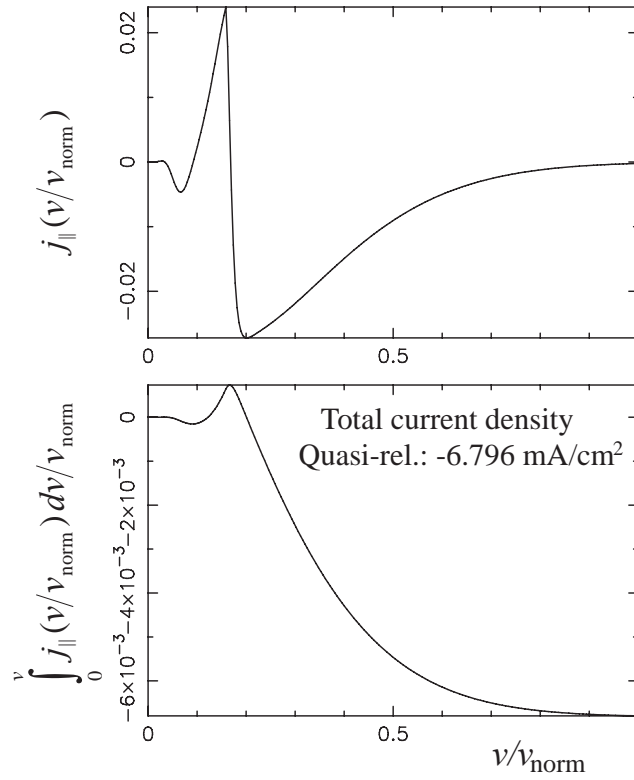


Fig. 25. LH-30keV test: Parallel current density as a function of normalized momentum, and corresponding cumulative value. Obtained with quasi-relativistic collision operator.

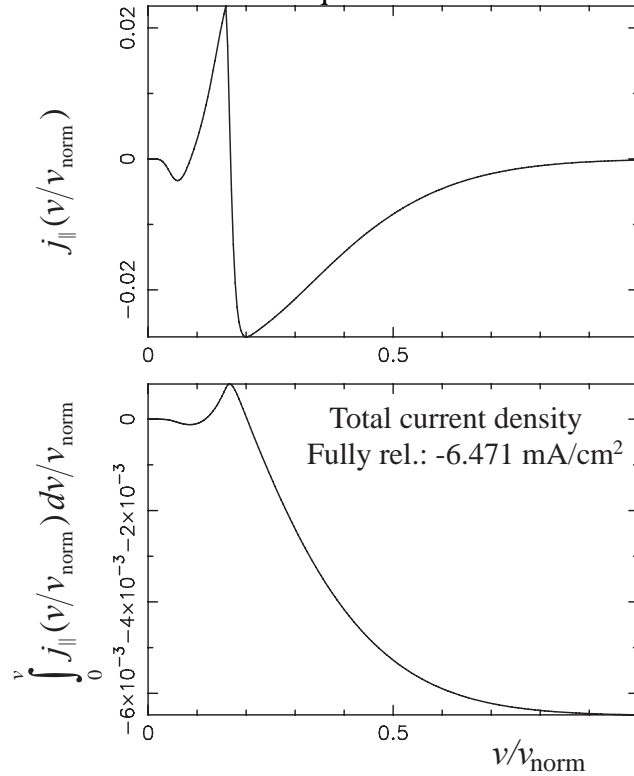


Fig. 26. LH-30keV test: Same as previous figure, but obtained with fully relativistic operator.

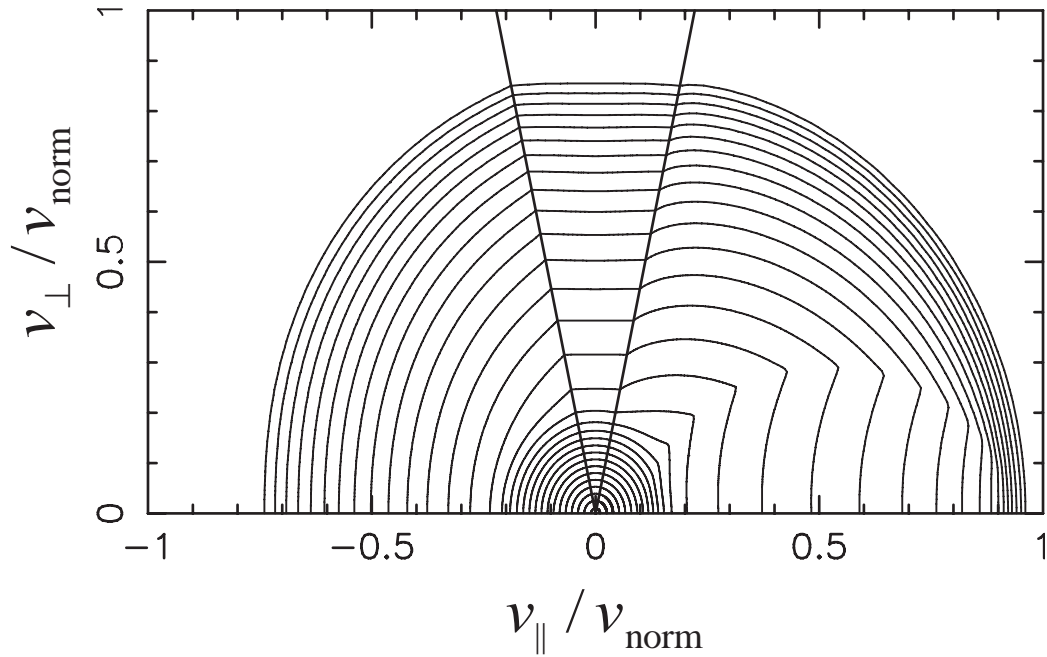


Fig. 27. ECH test: Contour levels of distribution function in momentum space obtained with fully relativistic collision operator; quasi-relativistic operator yields almost same result.

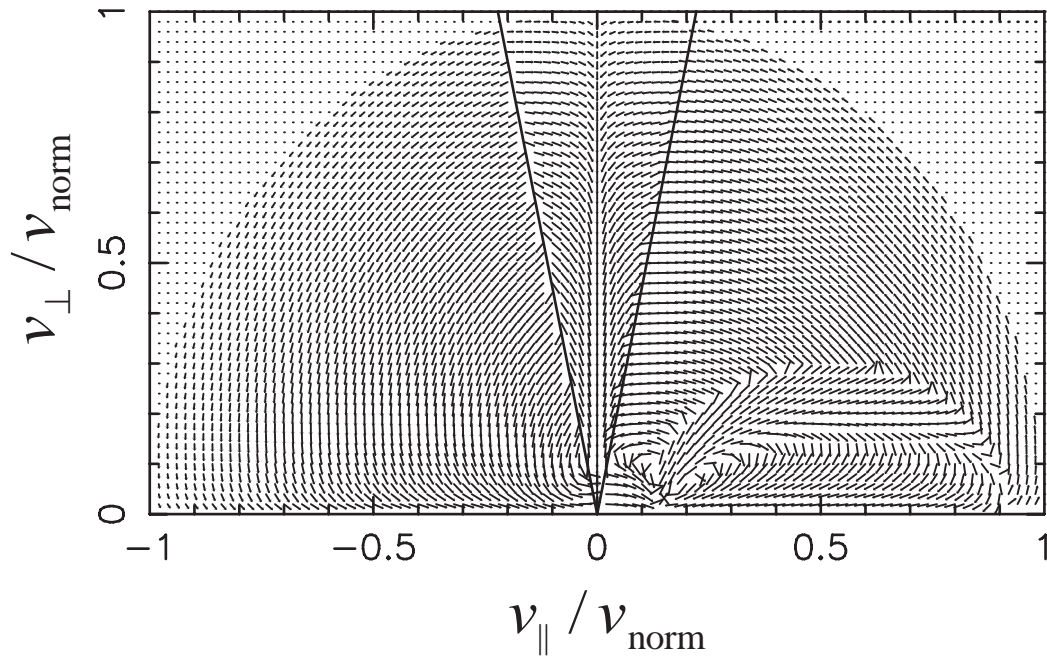


Fig. 28. ECH test: Total flux in momentum space obtained with fully relativistic collision operator (logarithmic scale); same result is obtained with quasi-relativistic operator.

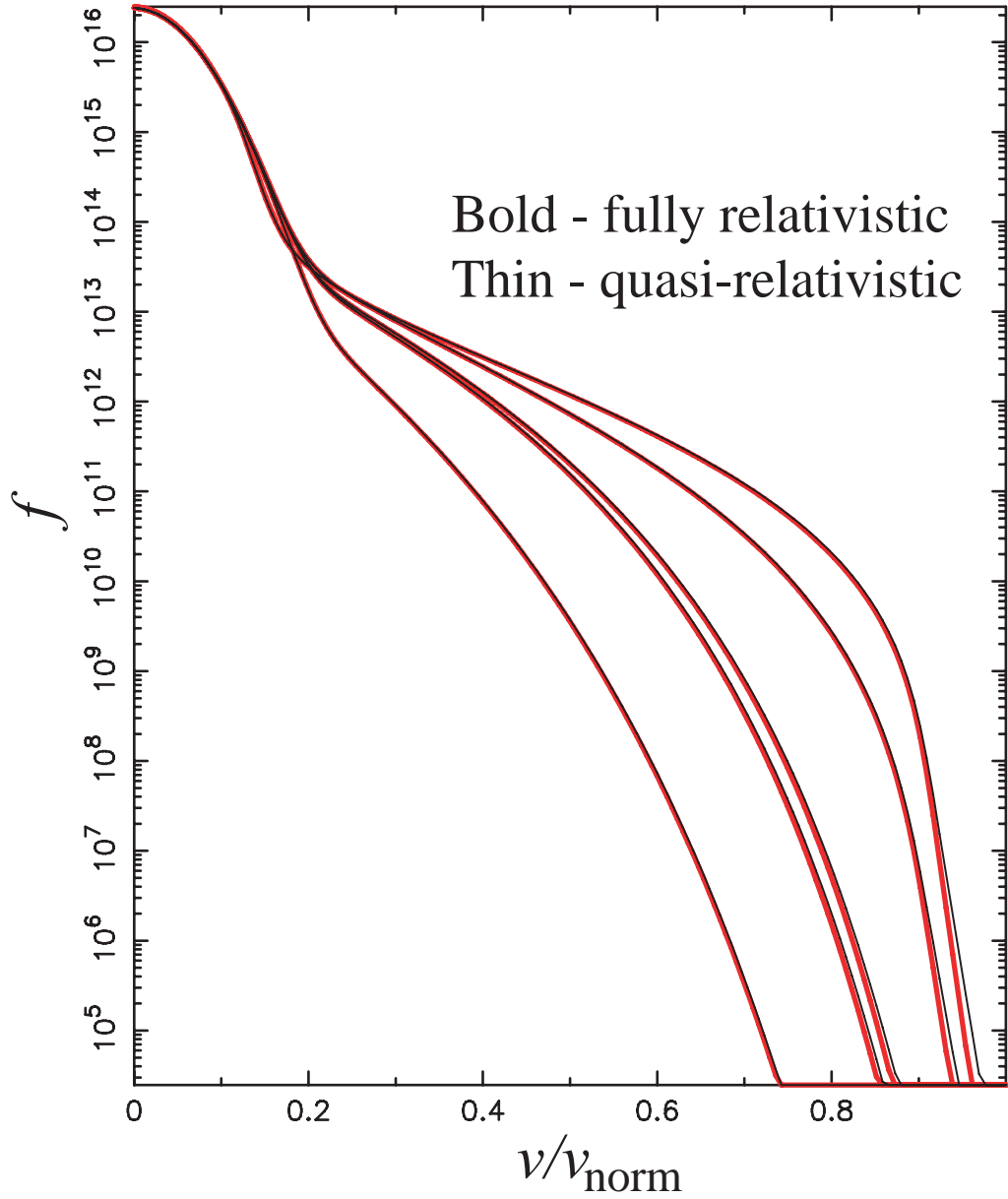


Fig. 29. ECH test: Cuts of distribution function vs. v/v_{norm} at different pitch angles.

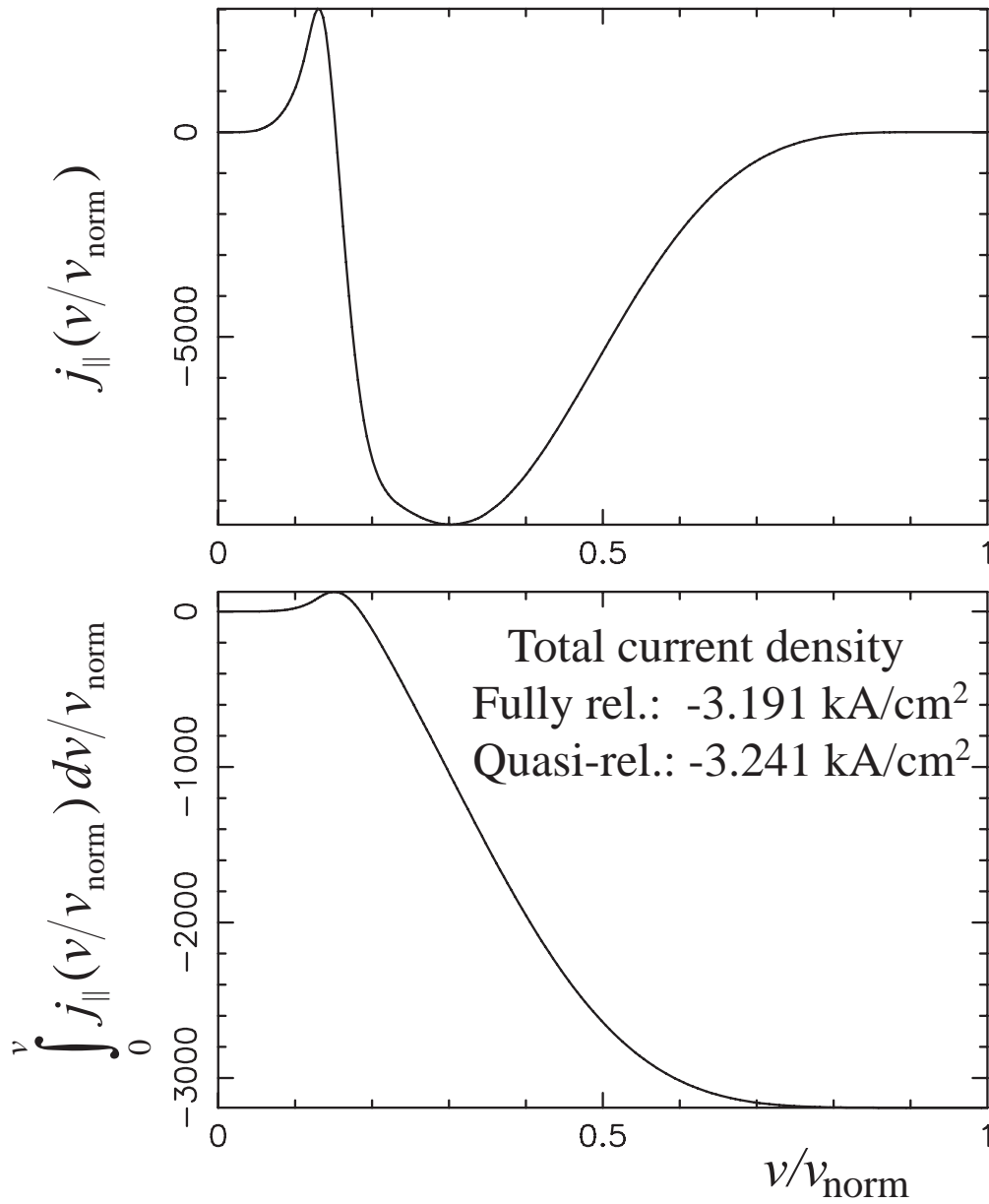


Fig. 30. ECH test: Parallel current density as a function of normalized momentum, and corresponding cumulative value. The result is almost the same for implementing fully-relativistic or quasi-relativistic operators.